LBNL-40630
Preprint

ERNEST ORLANDO LAWRENCE
BERKELEY NATIONAL LABORATORY

Mathematical Modeling of a Ponded Infiltration Test in Unsaturated Fractured Basalt at Box Canyon, Idaho

Christine Doughty

Earth Sciences Division

December 1998

Submitted to
Water Resources

REFERENCE COPY
Does Not
Circulate
Bldg. 50 Library - Ref.
Lawrence Berkeley National Laboratory
Copy 1
LBNL-40630

DISCLAIMER

This document was prepared as an account of work sponsored by the United States Government. While this document is believed to contain correct information, neither the United States Government nor any agency thereof, nor the Regents of the University of California, nor any of their employees, makes any warranty, express or implied, or assumes any legal responsibility for the accuracy, completeness, or usefulness of any information, apparatus, product, or process disclosed, or represents that its use would not infringe privately owned rights. Reference herein to any specific commercial product, process, or service by its trade name, trademark, manufacturer, or otherwise, does not necessarily constitute or imply its endorsement, recommendation, or favoring by the United States Government or any agency thereof, or the Regents of the University of California. The views and opinions of authors expressed herein do not necessarily state or reflect those of the United States Government or any agency thereof or the Regents of the University of California.

LBNL-40630

Mathematical Modeling of a Ponded Infiltration Test in Unsaturated Fractured Basalt at Box Canyon, Idaho

Christine Doughty

Earth Sciences Division
Ernest Orlando Lawrence Berkeley National Laboratory
University of California, Berkeley, CA 94720
e-mail: cadoughty@lbl.gov

December 1998

This work is supported by the Assistant Secretary for Environmental Restoration and Waste Management, Office of Technology Development, Characterization, Monitoring and Sensor Technology Program, of the U. S. Department of Energy under Contract No. DE-AC03-76SF00098.

LBNL-40630

Mathematical Modeling of a Ponded Infiltration Test in Unsaturated Fractured Basalt at Box Canyon, Idaho

Christine Doughty
Earth Sciences Division
Ernest Orlando Lawrence Berkeley National Laboratory

Abstract

Mathematical modeling of a ponded infiltration test conducted at the Box Canyon site in southeastern Idaho has been carried out to assess understanding of infiltration in a fractured basalt vadose zone and to evaluate the adequacy of conceptual and numerical models. A key question addressed is how the fracture-pattern geometry and fracture connectivity within a single basalt flow of the Snake River Plain basalt affect the pattern of water infiltration. The two-dimensional numerical model uses half-meter discretization to represent a 20 m by 20 m cross-section through the field site. The model extends from the ground surface to a perched water body, with explicit but highly simplified representation of major fractures and other important hydrogeologic features. The model adequately reproduces the majority of the field observations, confirming the notion that infiltration is largely fracture-controlled. Comparison to results obtained using a geostatistical approach to describe subsurface heterogeneity shows that information about fracture connectivity is lost in the construction of such stochastic representations, making them less successful at reproducing observed behavior.

1. Introduction

Ernest Orlando Lawrence Berkeley National Laboratory (Berkeley Lab), in collaboration with Idaho National Engineering and Environmental Laboratory (INEEL) and Stanford University, has recently concluded a project to study flow and transport in fractured basalt vadose zones, with the ultimate goal of improving performance of environmental remediation activities in such environments. The project focuses on concurrent development of a conceptual model and monitoring techniques for flow and transport; it includes field, laboratory, and modeling components. Field work is conducted at Box Canyon, located near INEEL in the Eastern Snake River Plain, Idaho. At the Box Canyon site, a clean site designed to serve as an analog for contaminated sites located within INEEL, a 25 by 25 m well field consisting of 38 vertical and slanted boreholes has been developed, and a 7 by 8 m infiltration pond has been constructed (Figure 1a). A nearby cliff-face exposure of the fractured basalt and minimal soil cover provide excellent views of the basalt flow structure, enabling extensive geologic mapping.

A hot air injection test, a series of air interference tests, and two ponded infiltration tests have been conducted at the Box Canyon site. The primary purpose of the hot air injection test was to identify and locate pathways for gas flow from the subsurface injection location (a packed-off interval of one borehole) to the ground surface, on the assumption that these same pathways would enable preferential liquid infiltration from the ground surface to depth and enable optimal placement of monitoring instruments for the subsequent infiltration test. No surface manifestation of the hot air injection test was observed, so this hypothesis could not be tested, but subsurface temperature changes were measured using strings of thermistors lowered into nearby open boreholes, enabling some subsurface gas flow paths to be mapped (Long et al., 1995). Subsequently, the air interference tests were conducted, to further identify preferential flow paths between different subsurface locations. Packer strings were used to isolate multiple intervals in several neighboring boreholes. Air was injected into one interval at a time while pressures were monitored in the other intervals. The goal is to combine the pressure responses to create a sort of tomographic image of gas flow paths between the boreholes. Analysis of the data is ongoing (Benito et al., 1998).

One of the factors complicating the study of infiltration and transport through the vadose zone of the Snake River Plain basalt is the sporadic nature of surface infiltration. The local precipitation rate is low, with major infiltration arising from seasonal snow melt and occasional intense summer storms. The ponded infiltration tests were conducted to study infiltration and transport under extreme boundary conditions, as might arise from large melt or storm events, and to provide a means of improving our understanding of infiltration and contaminant transport through the vadose zone toward the underlying Snake River Plain aquifer.

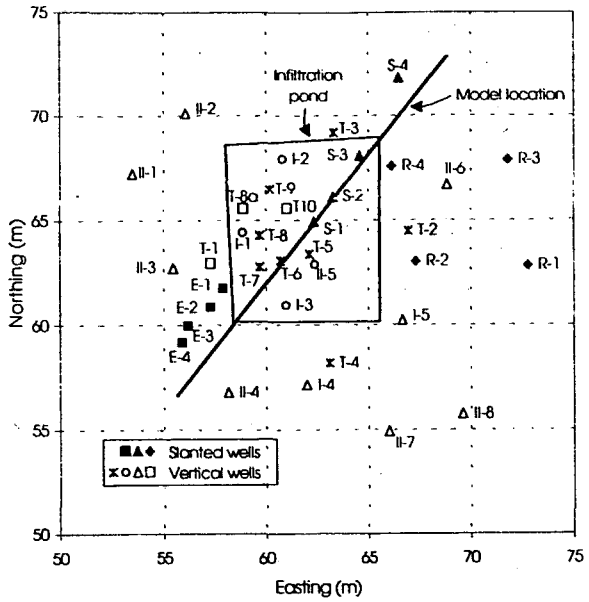

Figure 1a

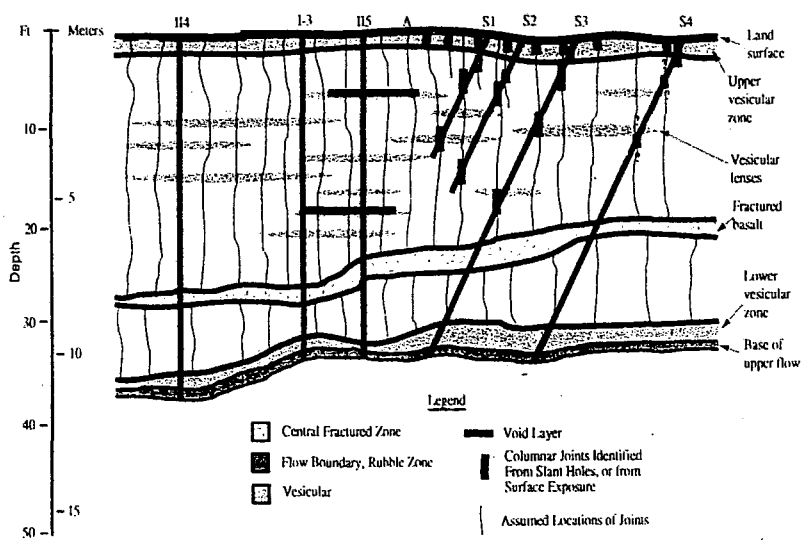

Figure 1b.

Figure 1. The Box Canyon field site. **(a)** Plan view showing the surface trace of the vertical cross-section model used for the ponded infiltration test. **(b)** Vertical cross-section through the field site, showing the upper of the two basalt flows modeled and the underlying rubble zone. Note that due to a lateral jog in the cross-section at the point A, Well II-5 is not as far from the S wells as it appears.

The present paper, which describes the numerical modeling of the first ponded infiltration test, is one of a series describing the results of the Box Canyon experiments. Faybishenko et al. (1999) describe a conceptual model for flow and transport through the fractured basalt, including a detailed description of the lithological components of the system. Peterson and Williams (1999) describe the use of ground penetrating radar to image both the site lithology and the infiltration process during the ponded infiltration test. Other project reports provide detailed descriptions of the data collected from the Box Canyon site (Long et al., 1995; Aydin and Lore, 1997; Faybishenko et al., 1998a, 1998b; Peterson and Williams, 1997; Benito et al., 1998; Grossenbacher and Faybishenko, 1995).

Mathematical modeling is done using a numerical simulator that calculates fluid flow through geologic media. Simulations are conducted prior to field tests to aid in experimental design, to study the importance of different factors affecting the test, and to predict the results of the tests in order to assess our understanding of the salient features of infiltration through a fractured vadose zone. Simulations are conducted after field tests to help explain the observed results, to assess the adequacy of the conceptual and numerical models, to infer the importance of various physical processes and the values of material properties, and to help design future tests.

One of the key questions addressed by modeling studies is how fracture-pattern characteristics and connectivity affect the pattern of water infiltration. For example, does flow occur predominantly through fractures or is matrix flow significant? Is vertical connectivity great enough to allow purely vertical infiltration with little lateral spreading, or does extensive spreading occur? Does entrapped air develop? A deterministic modeling approach is chosen over the more traditional stochastic approach to represent heterogeneity because there is a great deal known about the formation process and resulting geometric structure of the fracture patterns for the Snake River Plain basalt (e.g., Faybishenko et al., 1999; Aydin and Lore, 1997; Grossenbacher and Faybishenko, 1995). Correlated random field generators are deemed less capable of capturing the features of fracture connectivity that we believe are essential for modeling liquid infiltration realistically. Flow and transport through heterogeneous media may be studied at a variety of scales, ranging from laboratory to regional scales, and the choice of modeling approach certainly depends on the scale of interest. At the intermediate field scale of the Box Canyon site (tens of meters), we feel that we know enough about the hydrogeologic setting to be comfortable treating it deterministically.

Sections 2 and 3 describe the development and application, respectively, of the deterministic numerical model of the Box Canyon ponded infiltration test. Section 4 compares the results to those obtained using a traditional geostatistical approach, and Section 5 provides some concluding remarks.

2. Model Development

2.1 Physical Processes

The numerical simulator TOUGH2 (Pruess, 1987, 1991) is used for the present calculations. It is a general-purpose code that simulates two-phase flow of air and water in gaseous and liquid phases together with tracer and heat transport through porous or fractured geologic media, which may be strongly heterogeneous. TOUGH2 uses an effective continuum approach, in which fluid flow through both the fractures and rock matrix is assumed to be governed by Darcy's law. Relative permeability and capillary pressure functions are introduced to describe the interactions between liquid and gas phases. TOUGH2 was developed at Berkeley Lab and is widely used in the research community and consulting industry for a variety of problems including environmental remediation, geothermal and petroleum reservoir engineering, and nuclear waste isolation (Pruess, 1995, 1998).

TOUGH2 offers a variety of equation of state (EOS) modules to customize the code to the problem at hand. Two EOS modules are used for the present work: EOS3 and EOS9. EOS3 considers the fully coupled flow of water, air, and heat. Under two-phase conditions (typical for the unsaturated zone), the primary variables are gas-phase pressure P_g, gas-phase saturation S_g, and temperature T. Because we generally treat infiltration as an isothermal problem, we usually make use of an EOS3 feature that holds temperature constant and considers only two primary variables, P_g and S_g. EOS9 (Wu et al., 1996) is a simplified module that considers only liquid-phase flow under isothermal conditions, with the gas phase considered to be a passive spectator (Richards' equation). Under unsaturated conditions, the only primary variable required to specify the state of the system is liquid saturation S_l. For all EOS modules, the rock and all fluid phases are assumed to be in thermodynamic equilibrium within each grid block. Therefore, specification of the primary variables provides sufficient information to completely determine the state of the system. The Appendix presents the governing equations for flow and transport as formulated in TOUGH2.

2.2 Model Geometry

TOUGH2 uses the integral-finite-difference method (IFDM) for spatial discretization (Edwards, 1972; Narasimhan and Witherspoon, 1976), which offers greatly increased flexibility in grid design compared to typical finite difference methods. Grid blocks can be of arbitrary shape and size, and can be connected to as many neighboring grid blocks as desired. There need be no reference to a global system of coordinates, or to the dimensionality of a particular flow problem. For a regular lattice of grid blocks the IFDM is equivalent to a block-centered finite difference scheme, making it possible to simulate one-, two-, or three-dimensional rectangular geometries, or problems with radial, cylindrical, or spherical symmetry, in addition to more complicated irregularly arranged grid blocks.

The model for the Box Canyon ponded infiltration test is a two-dimensional vertical cross-section, which extends from the ground surface to a depth of 20 m, the approximate depth of a local perched water body. The model domain is uniformly discretized into 0.5 by 0.5 m square grid blocks. At this resolution, most individual fractures can be resolved, but the grid is too coarse to capture variability within a single fracture or to rigorously model interactions between fractures and the surrounding matrix. Hence, we focus primarily on infiltration through the fracture network, with matrix interactions approximately accounted for.

2.3 Model Representation of Geology

The geology at the Box Canyon site is typical of the Snake River Plain, and is primarily composed of highly fractured Quaternary basalt. Individual basalt flows are typically 3 to 12 m thick, and show an extreme elongation in one direction, giving them a finger-like structure with width typically ranging from 20 to 60 m. The surfaces of the basalt flow fingers are often so highly fractured as to be rubblized, while fracture density decreases toward the center of the flow fingers. The model is composed of an upper basalt flow finger, an underlying rubble zone, and the upper portion of a lower basalt flow finger. Figure 1a shows a plan view of the Box Canyon field site, with the location of the model identified. The model is aligned with the row of slanted boreholes called the S holes (Figure 1a). It underlies the NE-SW diagonal (10 m length) of the infiltration pond, and extends 5 m beyond the pond on both sides. This cross-section is chosen to make optimal use of the amount of geologic information available from boreholes. Figure 1b shows a schematic cross-section that is approximately aligned with the model, identifying the principal hydrogeological components of the upper basalt flow finger, developed from logs and cores taken from the vertical and slanted boreholes (for a detailed description of these components, see Faybishenko et al., 1999).

The numerical model, shown in Figure 2, includes explicit representation of the following features of the geological model shown in Figure 1b: 1) lens-shaped vesicular zones between depths of 0 and 6 m, 2) a central horizontal fracture zone at a depth of about 7 m, 3) non-vesicular massive basalt between depths of 7 and 10 m, 4) vesicular zones at the upper and lower margins of the basalt flow finger, and 5) a rubble zone at a depth of about 11 m.

Below the top of the rubble zone, the model becomes much less detailed, as fewer wells are available to constrain the lithology. The lithological log of Well II-5 (Long et al., 1995) indicates that the 3-4 m thick region of the model identified as the rubble zone is actually comprised of four rubble zones, each less than 0.3 m thick, separated by mostly vesicular, highly fractured basalt. These zones are combined for the numerical model, based on results of the hot air injection test (Long et al., 1995), which show that when hot air is injected at and just above the top of the rubble zone in Well S-3, temperature increases in Well II-5 are uniformly large over depths of 11-15 m, and decrease rapidly beyond those depths. Numerical modeling results (Long et al., 1995) suggest that such persistent temperature changes only arise when large, continuous gas-phase flow paths exist, allowing hot air to move in large quantities. Otherwise, the large heat capacities of

persistent temperature changes only arise when large, continuous gas-phase flow paths exist, allowing hot air to move in large quantities. Otherwise, the large heat capacities of rock and water compared to that of air cause the hot injected air to cool rapidly as it flows along small, isolated flow paths surrounded by cold, wet rock.

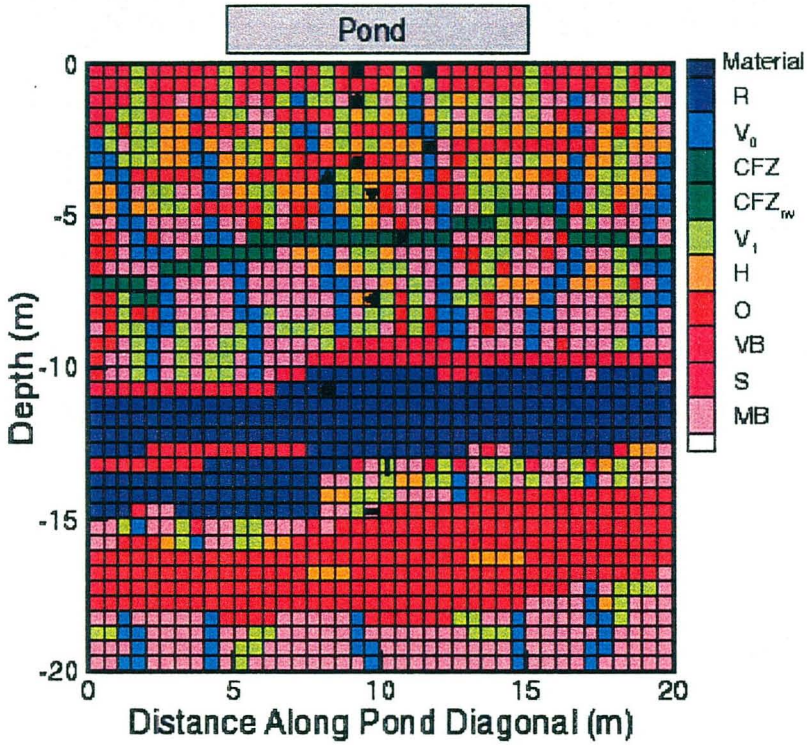

Figure 2. Two-dimensional vertical cross-section model used for simulating the ponded infiltration test. Material names and properties are given in Table 1. Locations at which transient responses are monitored are identified with black symbols.

Fracture pattern is particularly difficult to infer from borehole measurements, and the simple vertical fracture pattern shown in Figure 1b is not believed to be realistic. Therefore, the model incorporates the general pattern of column-bounding and column-normal fractures observed in outcrops at the Box Canyon site and throughout the Snake River Plain. Fracture spacing generally increases with distance from the top and bottom edges of basalt flow fingers (Faybishenko et al., 1999; Aydin and Lore, 1997; Grossenbacher and Faybishenko, 1995), as shown in the fracture map of the upper basalt flow exposed in the Box Canyon cliff face (Figure 3). A 20 m wide section of this map is superimposed on the TOUGH2 grid, and grid blocks underlying fracture traces are assigned as fracture grid blocks. A hierarchical structure has been developed to categorize the fractures (B. Faybishenko, personal communication, 1996), in which column-bounding fractures that extend all the way through the basalt flow finger are

denoted primary vertical fractures, shorter column-bounding fractures are secondary vertical fractures, the column-normal fractures connecting primary vertical fractures are primary horizontal fractures, and so on. Fracture permeability and porosity values are assigned to the model based on a simplified version of this structure, as given in Table 1. Soil infilling in shallow fractures that is observed in boreholes and at the ground surface is also included in the model, by assigning soil properties to near-surface fracture elements.

There are several limitations of the present representation of fractures within the vertical cross-section model. Firstly, although we believe that the general structure of the fracture pattern mapped at the Box Canyon cliff face represents the fracture pattern underlying the infiltration pond correctly, specific locations for individual fractures are very likely to be wrong. This is because the distance from the cliff face to the infiltration pond is about 30 m, whereas the maximum extent of fractures perpendicular to the cliff face is probably less than 5 m (the maximum observed fracture spacing along the cliff face is about 5 m and the fracture pattern is expected to be isotropic in plan view). Therefore, the model cannot make detailed predictions for individual point observations. It can, however, be used to predict behavior at 'generic' locations, for example the time-dependence of wetting for a location adjacent to a primary vertical fracture. The model can also be used to study the effect of different parameters and processes on the spatial variability of the infiltration process.

Secondly, although the model is finely enough discretized to identify individual grid blocks as either representing fracture or matrix (grid block dimension is 0.5 m, with fracture spacing ranging from 0.5 to 5 m), it cannot account for fracture variability within the 0.5 m grid block width. Thus, the model does not allow a rigorous treatment of flow within a fracture, in which apertures may range from microns to millimeters, or fracture/matrix interactions, which also require fine discretization of the matrix adjacent to the fractures. Instead, an effective continuum approach is used, in which grid blocks that represent a fracture actually encompass the 0.5 m wide zone of basalt in which the fracture lies. For a vertical fracture, the grid block is assigned a large vertical permeability to account for flow through the fracture, a small horizontal permeability to limit fracture/matrix flow, and a small porosity to account for the small aperture of the fracture. For a horizontal fracture, the permeability assignment is reversed. The use of a coarse grid to represent fracture/matrix interactions is similar to the traditional dual-porosity approach (Barenblatt et al., 1960; Warren and Root, 1963). This approach has been shown to produce erroneous results for some transient processes (Doughty, 1998), and more rigorous treatments involving finer matrix discretization are currently under development.

Three Dimensional Schematic of Cliff Face and Experimental Site

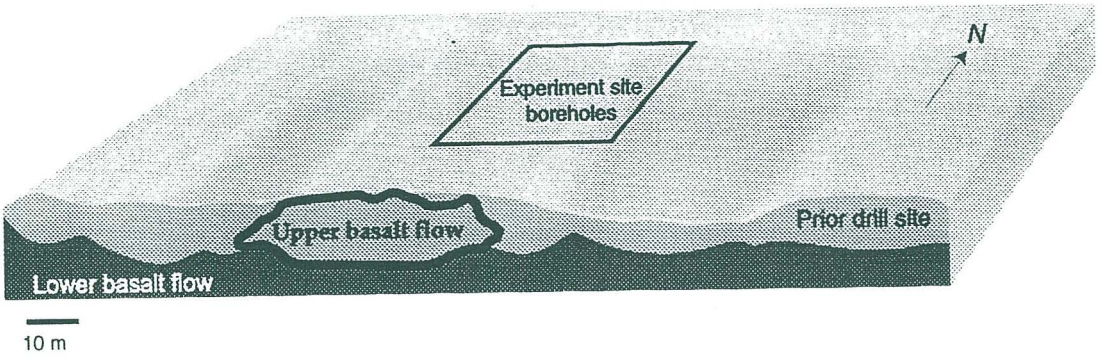

Fracture Map of Upper Basalt Flow

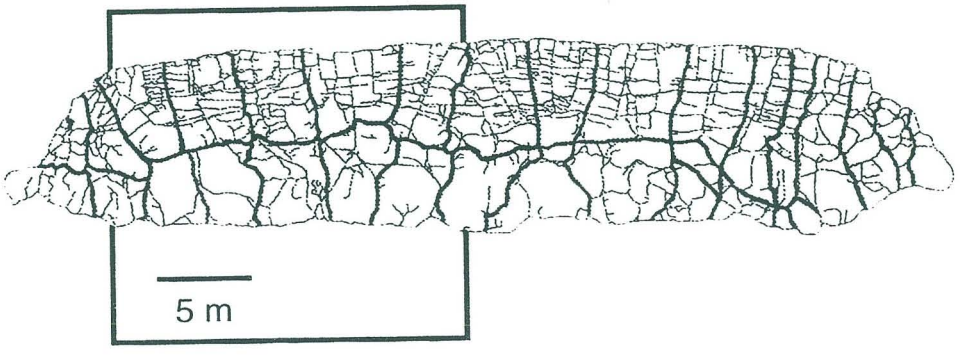

Figure 3. Fracture pattern mapped in the upper basalt flow finger at the Box Canyon cliff face exposure near the ponded infiltration test site (after Aydin and Lore, 1997). Primary (through-going) vertical fractures and the central fracture zone are shown bold. The border of the numerical model is shown superimposed on the fracture map.

dimensional model rather than a three-dimensional model is motivated by several practical issues. Computational requirements for running a three-dimensional model of comparable extent and resolution to the present two-dimensional model, while technically feasible with present computing resources, would become burdensome. Similarly, construction of the two-dimensional model as described above is very time-consuming; using the same procedure for a three-dimensional model (with 40 times as many grid blocks) would probably not be a worthwhile at this stage. Development of a more automated mesh generator is a possibility for future studies, but in the meantime, we justify the two-dimensional representation by noting that the fracture pattern is isotropic in plan view, so omission of the third dimension does not cause any qualitatively different behavior to be lost, and lateral flow should be minimal beneath the center of the infiltration pond, where the model is centered.

Finally, the values chosen for fracture grid block permeabilities and porosities are highly uncertain, even when taken in the context of effective medium properties for a coarse two-dimensional grid. Essentially, we consider the properties shown in Table 1 to be initial guesses, to be improved by comparing model predictions to observed data.

3. Model Applications

Prior to the ponded infiltration test, the model was used to simulate the test, in order to provide a baseline prediction against which field observations could be compared. Such a comparison allows us to assess the state of our knowledge prior to the test, and use test results to identify shortcomings in the model. Additionally, sensitivity studies were performed to investigate the impact of some poorly known hydrologic properties. Because it was unknown *a priori* if the results of the unconventional 'quasi-deterministic' modeling approach used for the fracture network would bear any resemblance to field observations, the pre-test simulations were kept relatively simple.

As data from the ponded infiltration test began to be evaluated, it became apparent that the numerical model of the infiltration test did provide useful results, but that it would benefit from the inclusion of additional physical processes. Therefore, a series of post-test simulations was done, in which additional features were added and certain aspects of the model were calibrated to observed behavior.

3.1 Pre-Test Calculations

Processes Modeled

Two alternative approaches are taken during pre-test studies. The first uses the traditional soil physics approach, in which air is a passive spectator, and liquid saturation is the only variable to be calculated. The EOS9 module of TOUGH2 implements this approach. The second, more rigorous, approach is to consider the fully coupled two-phase flow of water and air, which can be done using the EOS3 module of TOUGH2, and requires calculating both gas pressure and liquid saturation. The primary motivation for using EOS9 is numerical efficiency. The addition of air to infiltration problems can cause severe numerical difficulties, especially for highly heterogeneous media, because liquid-phase and

gas-phase processes occur on very different time scales. The primary motivation for using EOS3 is that it allows the development of entrapped air, which is believed to be an important effect for infiltration into heterogeneous media (Faybishenko, 1993, 1995). In most of the EOS3 calculations described in this section isothermal conditions are assumed, which eliminates the need to solve the energy balance equation, making the numerical simulations more efficient.

In the absence of any field data from which to derive the dependence of relative permeability on saturation, Corey (1954) curves (see Appendix) are used. Corey curves are chosen because of their simple functional form and because the sum of liquid and gas-phase relative permeability is much less than one, implying that there is strong interference between the two fluid phases. Strong interference is considered reasonable for flow in fractured media, because flow geometry is generally more restricted than in three-dimensional porous media. For the EOS9 calculations, the Corey curve is used for k_{rl} and k_{rg} is not needed (it is infinite by definition).

Capillary pressure is set to zero in most of the pre-test calculations. Thus, there is no capillary force driving liquid from wet to dry regions, and liquid flows in response to gravity only (EOS9) or a combination of gravity and gas-phase pressure gradients (EOS3). This simplification is made because there is no data available to specify capillary pressure-liquid saturation relations for the fractured basalt at Box Canyon, although fracture capillary pressures are commonly assumed to be small. In reality, flow paths and moisture distributions develop in response to a combination of gravity and capillary forces, with gravity acting to localize flow in high permeability vertical pathways and capillary forces spreading moisture to lower permeability regions diffusively. By ignoring capillary forces, we produce a sharp picture of preferential flow paths, which is consistent with our main goal to investigate the impact of different hydrologic components on the spatial distribution of the infiltrating water. Ultimately, we hope to use the results of laboratory and field infiltration tests, in conjunction with inverse modeling, to infer appropriate characteristic curves for the Box Canyon site. A simplified version of this procedure is demonstrated in the post-test calculations, which do include capillarity.

Initial and Boundary Conditions

For the EOS9 calculations, the initial condition is a uniformly partially-saturated medium with liquid saturation $S_l = 0.1$, in which water is immobile (residual liquid saturation S_{lr}=0.12). For the EOS3 calculations, a gas-static pressure profile is also specified. In both cases, temperature remains constant at 10°C.

The pond boundary is represented by a liquid-saturated, constant-pressure boundary at 0.3 m of head, corresponding to the planned depth of water in the pond. For the EOS3 calculations, a constant pressure boundary representing the atmosphere overlies the non-pond portion of the model upper boundary, whereas for the EOS9 calculations this is a closed boundary. Lateral and lower boundary conditions are constant saturation (and constant pressure for EOS3). Lateral boundaries are open to liquid flow (and gas flow for EOS3) and the lower boundary, which represents a local perched water body, is open to liquid flow. Ponding lasts for four weeks.

Simulation Results

Two base-case simulations are done, one with EOS9 and one with EOS3. Then a series of sensitivity studies is carried out, in which some of the more uncertain input parameters are varied.

Base-case simulations. Figures 4 and 5 show the predicted change in liquid saturation distribution from the initial state and the liquid flow field at a series of times for the EOS9 and EOS3 base cases, respectively. In both cases, the infiltration does not proceed uniformly, but follows highly irregular paths, bypassing the massive basalt sections, and focusing in the high-permeability fractures. Consequently, the tributary structure of the fracture pattern (Figure 3) causes a funneling of the infiltrating water, which is particularly apparent below the central fracture zone (6-7 m depth). Several types of field observations made during the ponded infiltration tests support a funneling of flow as depth increases (Faybishenko et al., 1999), which is consistent with the model results. Along with this funneling, a moderate amount of lateral spreading occurs, with the overall plume width increasing from its original 10 m to about 15-18 m near the bottom of the model. The primary avenues for lateral flow are vesicular lenses, the central fracture zone, and the rubble zone. Flow through most of the rubble zone (11-14 m depths) is purely vertical, with lateral spreading occurring only along the bottom margin. This is an artifact of the uniform structure used for the modeled rubble zone. If the actual alternating layers of rubble and fractured basalt were included, lateral flow could occur at the base of each rubble zone. However, even with this added complexity, lateral flow would not persist for great distances, only until the next high-permeability vertical flow path were encountered, as is seen in Figures 4 and 5.

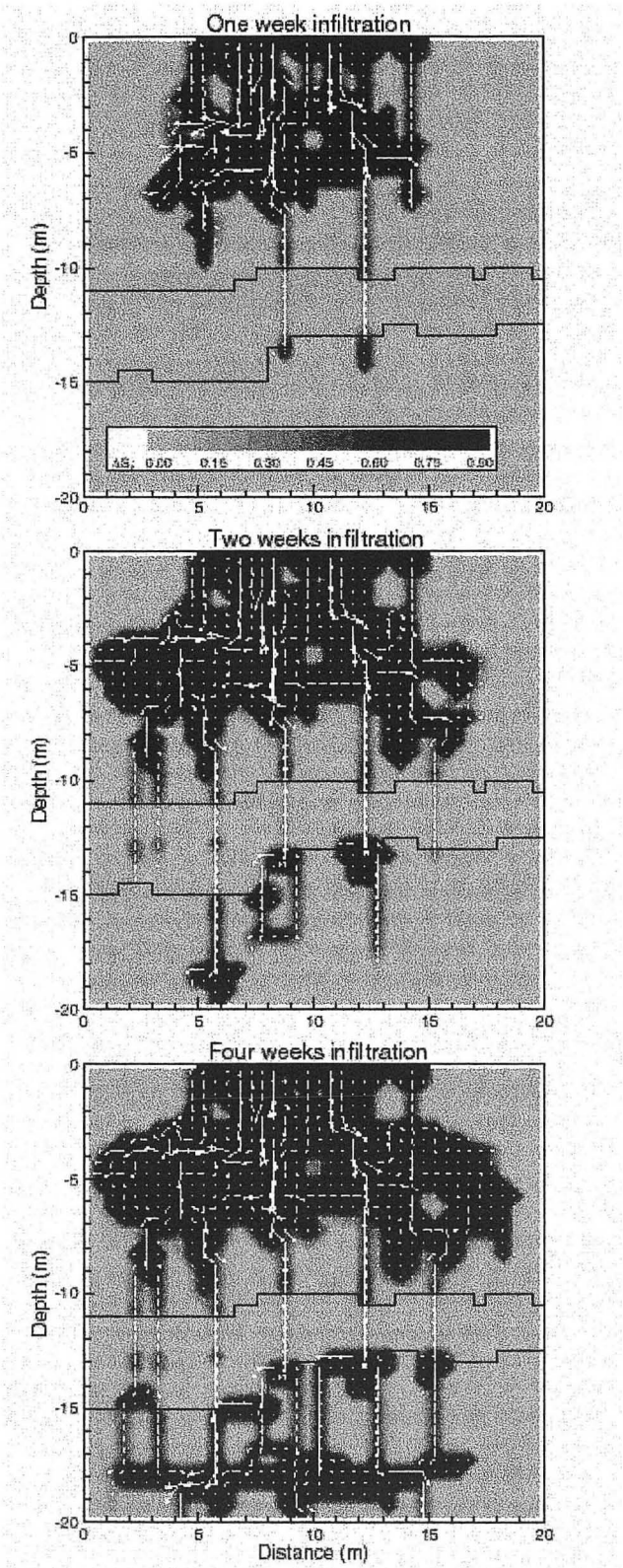

Figure 4. Simulated change in liquid saturation from the initial state (S_l=0.1) and liquid flow field at a series of times during the infiltration test, for the EOS9 pre-test base case calculation. The infiltration pond and rubble zone boundaries are also shown.

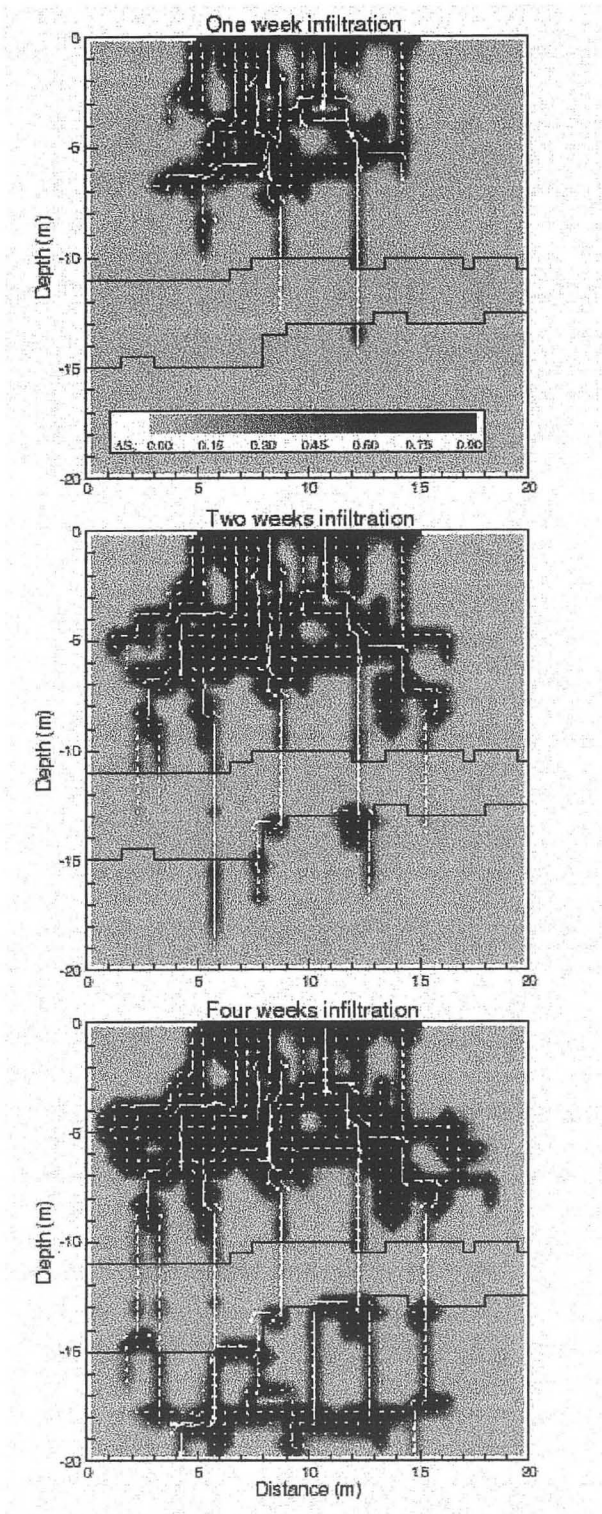

Figure 5. Simulated change in liquid saturation from the initial state (S_l=0.1) and liquid flow field at a series of times during the infiltration test, for the EOS3 pre-test base case calculation.

Figure 6 compares the infiltration rate from the pond with the simulated values for the two base cases. The method used to determine the observed infiltration rate data is described in Faybishenko et al. (1999). For a ponded infiltration test conducted in a heterogeneous, initially partially saturated medium, the infiltration rate is expected to decrease with time for several reasons. According to Darcy's law, flow is proportional to the sum of the pressure gradient and the gravity force. At early times, the pressure gradient imposed by suddenly ponding water is huge (the pressure profile is initially a step function), so infiltration rate is high. The magnitude of the step function depends on both the height of ponding and the magnitude of capillary pressure under natural (partially-saturated) conditions. As time passes, the pressure gradient decreases as the wetting front advances and consequently so does the infiltration rate. Eventually the front moves far enough away so that the pressure gradient becomes negligible compared to the gravity force, and in a homogeneous medium infiltration rate becomes steady. Infiltration rate would continue to decrease if the infiltrating plume moved from a high to low permeability region. Strongly heterogeneous media (even those without a systematic depth trend in permeability) tend to show a greater decrease in infiltration rate with time than do homogeneous media, as large high-permeability flow paths that are accessible from the ground surface fill rapidly, leading to a large initial infiltration rate.

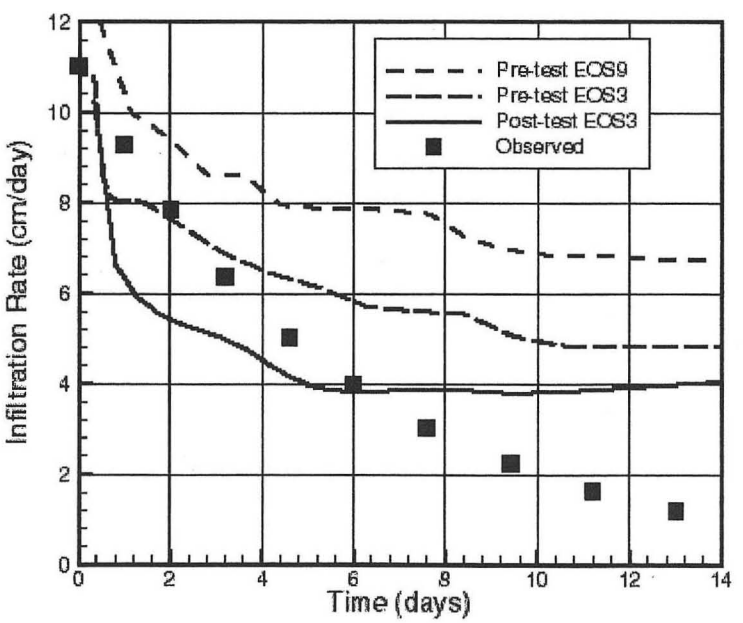

Figure 6. Comparison of simulated and observed infiltration rates for the pre-test and post-test calculations.

The general trend of decreasing infiltration rate is reproduced by the model for both the EOS3 and EOS9 cases, but the simulations show a smaller overall decrease in infiltration rate than is observed in the field. Sensitivity studies described in the next section indicate that by varying flow parameters, the modeled infiltration rate curve can be shifted up or down, but the shape of the curve never changes enough to match the observed curve closely. This discrepancy could indicate a fundamental shortcoming of the model. However, it is also possible that an early-time under-prediction of infiltration rate by the model arises because of leaks that existed in the pond during the first few days of the test, resulting in a larger area available for infiltration than in the model. Furthermore, the late-time over-prediction of infiltration rate by the model may be the result of decreased permeability caused by clogging of flow paths by fine materials, another process believed to be occurring in the field that is not included in the model.

The EOS3 simulation yields significantly different results than does the EOS9 simulation, suggesting that entrapped air plays an important role and needs to be included in the model. Although the infiltrating water generally finds the same preferential pathways for the EOS9 and EOS3 simulations (compare Figures 4 and 5), more regions are bypassed by liquid water with EOS3. The saturation distribution is thus much less uniform when entrapped air develops. Subsurface flow rates are also smaller due to the enhanced flow resistance caused by pressure buildups due to entrapped air. The total infiltration rate from the pond is consequently smaller as well (Figure 6).

Figure 7 compares the transient response to ponding for the EOS3 simulation at selected locations in the model to observed values in wells T-5 and T-9. The model locations cannot be exactly identified with wells T-5 and T-9, because the model is not that precisely defined (recall that the fracture pattern is taken from the cliff face exposure 30 m away), and in any event, Wells T-5 and T-9 are offset from the pond diagonal with which the model is aligned (Figure 1a). The model locations (shown in Figure 2) are chosen to match the lithology observed in Wells T-5 and T-9 at the depths of the sensors, in order to provide representative model results. The observed data show capillary pressure, P_c, which is not included in the model, so liquid saturation, S_l, is plotted instead. Without assuming an explicit form for $P_c(S_l)$, a quantitative comparison of modeled and observed results is not possible, but a qualitative comparison can be made merely by assuming that $P_c(S_l)$ is a continuous function, as described below.

Prior to the start of ponding, all observed pressures are negative, indicating unsaturated conditions prevail. At the 0.3 m depth in both wells, where lithological logs (Faybishenko et al., 1998a) indicate moderately permeable vesicular basalt is found, the observed data show a rapid pressure increase when ponding begins, followed by a steady positive pressure, indicating a rapid transition to saturated conditions. The corresponding modeled responses also show a rapid increase to steady near-saturated conditions. There is no observed or modeled response at the 1.5 m depth in well T-5, where low-permeability massive basalt is apparently bypassed by the flow. The small, gradual pressure increase observed in well T-5 at 3 m occurs in vesicular basalt and is well matched by the slow saturation increase in the model. There is a strong, oscillating pressure response observed in well T-9 at 1.5 m, where the lithological log identifies a fracture. A response with similar characteristics is seen in the model in a primary vertical

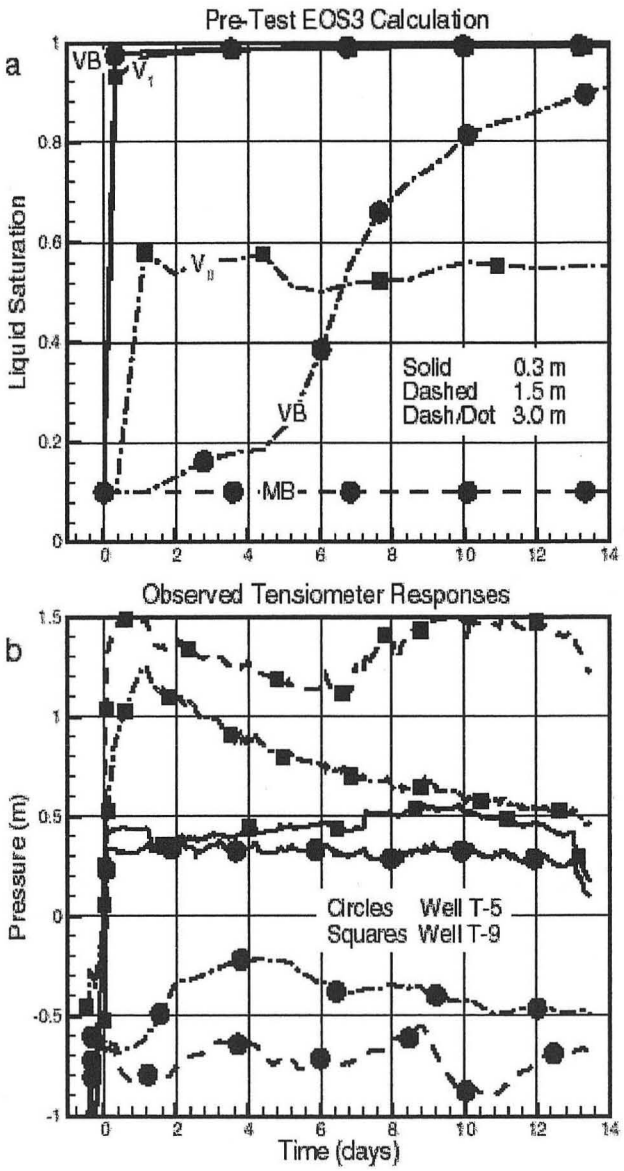

Figure 7. Comparison of (**a**) simulated and (**b**) observed transient responses to ponded infiltration at locations representing wells T-5 and T-9 (circles and squares, respectively, in Figure 2), for the EOS3 pre-test base case calculation. The model material in which each response occurs is also shown in Figure 7a.

fracture at the 3 m depth. The oscillations likely occur as the downward-moving plume encounters large changes in permeability, arising from openings or constrictions in fracture flow paths. The pressure response observed in Well T-9 at 3 m also suggests a fracture in which a steady flow regime does not develop. After a large, early pressure response indicating rapid water arrival, the gradual pressure decline suggests that the fracture begins to drain and thus that this location does not remain part of the main network of preferential flow channels. This type of behavior is not observed in the model, but overall, the model captures most of the different kinds of transient behavior observed in the field.

Sensitivity studies. Table 2 summarizes the sensitivity studies conducted, and shows the predicted infiltration rate from the pond for each one. Parameters that are studied include fracture transmissivity and effective porosity, the vertical extent of fractures near the ground surface and below the rubble zone, and the relative permeability functions used. The infiltration rate ranges from 5 to 33 cm/day, depending primarily on the transmissivity assumed for the largest vertical fractures. The shape of the infiltration rate curves are all similar to those for the base-case simulations, shown in Figure 6.

When air relative permeability is increased (Case 17) or the interference between liquid and gas phases is lessened (Case 26), the effect of entrapped air decreases and infiltration rate increases. The values of infiltration rate intermediate between Cases 13 (no air entrapment) and 16 (full air entrapment) are reasonable for these partial air entrapping conditions.

If fractures do not extend to the ground surface (Case 18 compared to Case 13), the infiltration rate from the pond decreases significantly. A decrease in fracture porosity (Case 19 compared to Case 13) does not affect infiltration rate, but does shorten the arrival times of the water at various depths in the model. Increasing fracture permeability by a factor of 10 (Case 20 compared to Case 13) greatly increases infiltration rate, well beyond the observed values, providing information on the range of actual fracture permeabilities.

The lack of widespread lateral flow at the base of the rubble zone is somewhat surprising, given results of a large-scale infiltration test conducted by INEEL in 1994 at a site several km away from Box Canyon. In that test, lateral flow in a rubble zone overlying a sedimentary interbed persisted for at least 100 m (Wood and Norrell, 1996). Two variations in the Box Canyon model are considered. In the first (Case 24), permeability just below the rubble zone is decreased by converting fracture grid blocks to soil-filled fracture grid blocks, which results in about a factor of ten decrease in the highest permeabilities underlying the rubble zone. This change has almost no effect on the model results. In the second variation (Case 25), all grid blocks underlying the rubble zone are converted to massive basalt, resulting in the complete cessation of vertical flow beneath the rubble zone. Rather than reaching the perched water body, infiltrating water is diverted laterally along the base of the rubble zone and exits the model through a lateral boundary. This finding suggests that the permeability of the sedimentary interbed noted in the 1994 test must be very low, and that the interbed itself must be continuous for such widespread lateral flow to occur.

A non-isothermal calculation (Case 22), in which the pond water is maintained at 20°C (due to solar heating), produces saturation distributions that differ from the base case (Case 16) only slightly, but results in a 30% higher infiltration rate because of the temperature dependence of the viscosity of water, $\mu(T)$ ($\mu(20)/\mu(10) = 1.3$). The inclusion of non-zero capillary pressure (Case 28 compared to Case 13) creates a much more diffuse plume, with gradual variations between wet and dry regions, but the infiltration rate does not change, suggesting that while capillary forces play an important role in determining the distribution of water in the subsurface, they are not the controlling factor in determining the rate of infiltration from the pond.

3.2 Post-Test Calculations

Processes Modeled

During the ponded infiltration test, gas bubbles were observed in the pond, indicating that air can become entrapped (and subsequently released) beneath the pond, rather than simply being purged by the infiltrating water. Therefore, we consider the fully coupled two-phase flow of water and air, using the EOS3 module of TOUGH2. Because temperature effects were shown to be minor in the pre-test sensitivity study described above, isothermal conditions are assumed here, eliminating the need to solve the energy balance equation. We attempt to improve on the realism of the modeled saturation distribution by including non-zero capillary pressures using the van Genuchten (1980) formulation. We impose a background (natural-state) infiltration rate, then determine the magnitude of the capillary pressure strength by calibrating the natural-state conditions predicted by the model to rough estimates of capillary pressure and saturation made prior to the ponded infiltration test. This represents a significant additional complexity compared to the pre-test calculations, which include either air flow or capillary pressure, but not both, and never attempt to develop realistic natural-state conditions.

Initial and Boundary Conditions

The initial conditions for the ponded infiltration test are determined by running a natural-state simulation in which gravity and capillary forces come to equilibrium in the presence of a background infiltration rate. This procedure results in a stable moisture distribution, so the only subsequent saturation changes that occur are those arising from the infiltration test.

The constant-pressure boundary at the pond is set to 0.23 m of head, corresponding to the actual water depth during ponding. Boundary conditions for the atmosphere, lateral model boundaries, and the perched water body underlying the model are the same as for the EOS3 pre-test calculations. The background infiltration continues throughout the test.

Simulation Results

<u>Developing a robust model.</u> For the pre-test calculations in which no capillary pressure is included in the model, switching from EOS9 to EOS3 causes no difficulty other than requiring about an order of magnitude more computer time for each simulation. The

addition of capillary pressure with the EOS9 module is somewhat more problematic, with the ability of the code to run successfully somewhat dependent on initial conditions. An even greater numerical challenge arises when trying to use capillary pressure with the EOS3 module. The choice of relative permeability curves strongly impacts the ability of the code to run, with strong phase interference and in particular low gas-phase relative permeability required. Using different relative permeability curves results in different infiltration rates from the pond, requiring a calibration procedure. Ultimately, power-law relative permeability functions with an exponent of n = 5 are found to satisfy both the requirement for a robust enough model to simulate the entire infiltration test and a reasonable match to the observed infiltration rate.

Natural-state model. Rough estimates of capillary pressure (1-3 m suction, i.e., –0.1 to –0.3 bars of pressure) and liquid saturation (70 to 90 percent) based on field observations made prior to the ponded infiltration test (B. Faybishenko, personal communication, 1996) are assumed to represent natural-state conditions and are used to constrain the capillary pressure strength P_{c0} of each of the materials in the model, as described below. In order for the magnitude of capillary pressure not to increase linearly from the water table, a background infiltration rate is required. The magnitude of this infiltration rate is unknown *a priori*, but may be somewhat constrained by local meteorological data (e.g., it is probably less than the local precipitation rate). The background infiltration rate is assigned as a mass source term to the uppermost active (i.e., non-boundary) grid blocks of the model, which are assigned a large horizontal permeability to allow the infiltrating water to redistribute itself. A gas-static pressure profile is imposed by holding pressure fixed at the upper and lower boundaries of the model.

Our starting guess for the capillary pressure strength of each material is to assume that it is inversely proportional to the square root of the geometric mean intrinsic permeability of that material. Because a natural state simulation using these P_{c0} values does not produce reasonable natural-state saturation or capillary pressure distributions, other P_{c0} values were tried and the natural-state simulation repeated. After several natural-state simulations, using capillary pressure strength and background infiltration rate chosen by trial and error, we arrive at the parameter set given in Table 1 and a background infiltration rate of 0.027 cm/day (10 cm/year) which produces the liquid saturation and capillary pressure distributions shown in Figure 8. All the model capillary pressures are within the observed range, but the liquid saturations tend to be lower than those observed, except in the massive basalts just above the rubble zone. We believe that the rubble zone and primary vertical fractures are relatively dry under natural conditions, since their high permeabilities are associated with weak capillary pressures, and this is adequately represented by the model. However, the vesicular basalt lenses and shallow soil layer should be wetter (0.7-0.8 rather than 0.3-0.4). In order to achieve this and at the same time maintain a reasonable match to the ponded infiltration rate would require introducing different relative permeability functions for different materials and a great deal more fine-tuning of parameters. Given the lack of hydrologic data available for the geologic materials at Box Canyon, and the overall simplicity of the numerical model, it is not considered worthwhile to attempt this at this stage. Despite its shortcomings, we believe that the natural-state model portrays a reasonable flow distribution, in which the

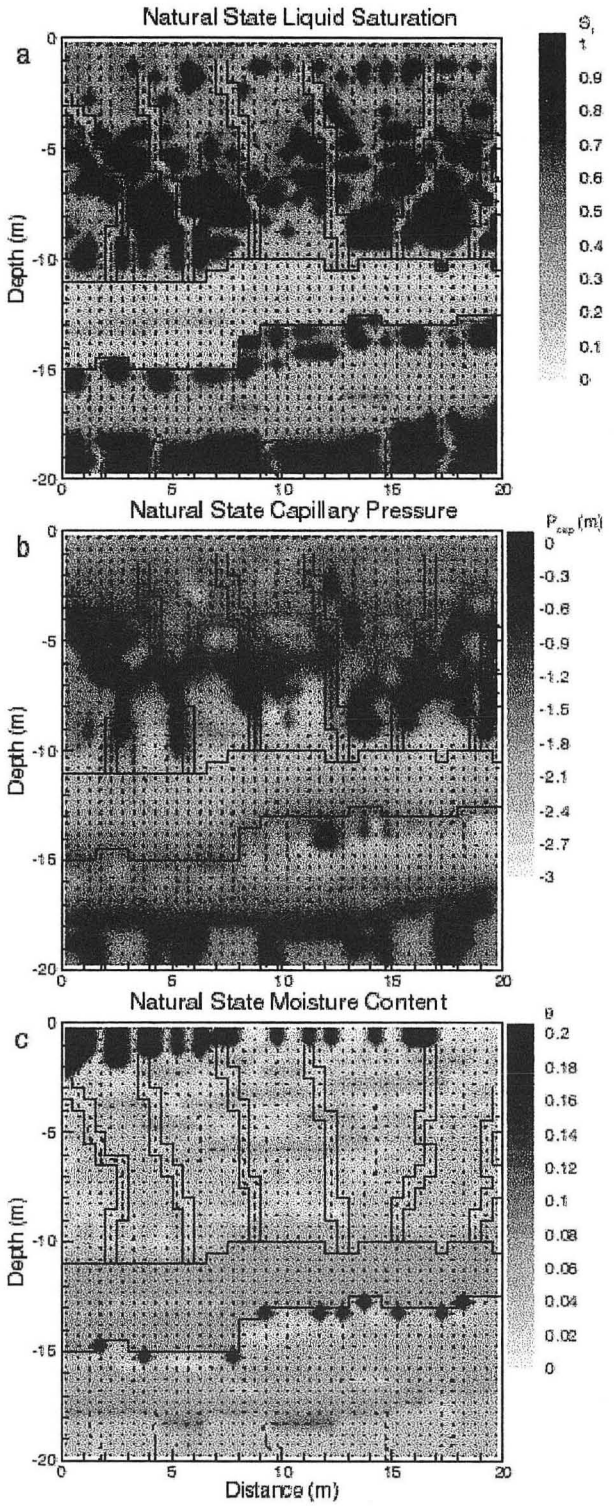

Figure 8. Simulated natural-state distributions of **(a)** liquid saturation, **(b)** capillary pressure, and **(c)** moisture content used as initial conditions for the EOS3 post-test calculation. A background infiltration rate of 10 cm/yr is imposed. The locations of the primary vertical fractures above the rubble zone and the liquid flow field are also shown.

primary through-going vertical fractures are not the main pathways for background liquid flow in the upper 7 m of the model, as their low liquid saturation makes their relative permeability lower than that of smaller vertical fractures. Instead, flow is widely distributed among all the vertical fractures in this depth range.

Figure 8 also shows the natural-state moisture content distribution θ, where $\theta = S_l\phi$, the product of liquid saturation and porosity. Moisture content is the physical variable to which geophysical methods such as neutron logging and ground penetrating radar are sensitive. Because of the large differences in porosity for the different hydrogeological components at Box Canyon, distributions of liquid saturation and moisture content may look quite different. In particular, the high porosities of the soil and rubble zone convert even small liquid saturations to significant moisture contents. The moisture content distribution shown in Figure 8 is consistent with neutron logging and ground penetrating radar surveys conducted prior to the infiltration test, which tend to show high moisture contents in the central fracture zone and rubble zone (Faybishenko et al., 1998b; Peterson and Williams, 1997).

Ponded infiltration test model. Figure 9 shows the simulated change in liquid saturation from the natural state (Figure 8) and the liquid flow field at a series of times during the ponded infiltration test. Compared to the EOS3 pre-test calculation (Figure 5), the post-test calculation shows much more gradual, widespread saturation changes than does the pre-test calculation, which is consistent with the addition of capillarity. However, the overall pattern of localized, preferential flow through vertical fractures, with lateral spreading through the subhorizontal high-permeability pathways afforded by vesicular lenses, the central fracture zone, and the rubble zone is present for both pre-test and post-test calculations, making the overall infiltration patterns similar. Within the rubble zone, vertical flow is much more uniformly distributed than for the pre-test calculation, another expected consequence of the addition of capillarity. Note that in the post-test calculation at $z = 3$ m, $x = 15$ m, enhanced lateral flow in a vesicular zone has made possible a completely new flow path, one that exits the model at a depth of about 4 m (compare the upper frames of Figures 5 and 9). Such large consequences of small changes in flow conditions are to be expected in strongly heterogeneous media, as described in Faybishenko et al. (1999).

Figure 9 shows that as in the pre-test calculations, lateral flow along the base of the rubble zone is not continuous over more than a meter or so, due to the presence of underlying vertical fractures that intercept the water. In contrast, in the field, perched water was observed at the rubble zone depth in wells up to 5 m away from the infiltration pond (Faybishenko et al., 1999), suggesting that more extensive lateral flow occurs through the rubble zone than is predicted by the numerical model. This in turn requires a greater extent of low-permeability material underlying the rubble zone than is present in the model. Such a layer could exist if fracture spacing beneath the rubble zone were greater than that suggested by the cliff-face fracture map, or if fractures existed but had lower permeability than indicated by core samples. In any event, such hydrological responses provide valuable means to improve the numerical model, in that they do not

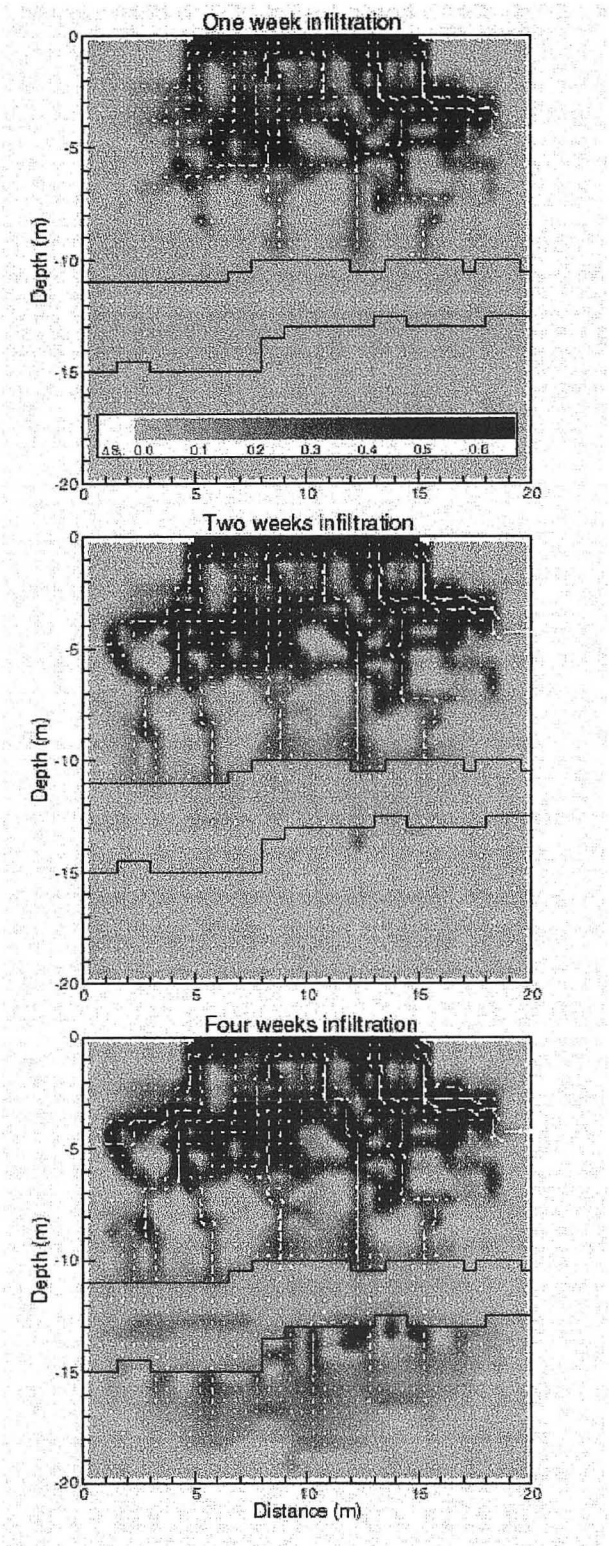

Figure 9. Simulated change in liquid saturation from the natural state (shown in Figure 8a) and liquid flow field at a series of times during the infiltration test, for the EOS3 post-test calculation. Note the change in saturation scale from Figures 4 and 5.

require either extrapolation (as do cliff-face observations) or interpolation (as do core-scale measurements), both of which operations are unreliable in highly heterogeneous systems..

Figure 10a shows the simulated liquid saturation distribution and the liquid flow field after two weeks of ponded infiltration. Showing the saturation distribution itself, rather than the change in saturation from the natural state as in Figure 9, enables the infiltration process to be seen in the same context the monitoring instruments in the field have. The liquid flow field shows that under ponded boundary conditions the primary vertical fractures provide the main pathways for liquid infiltration, in contrast to the background liquid flow field shown in Figure 8. Figure 10b shows the simulated change in moisture content from the natural state and the gas flow field. The primary differences between the saturation changes (Figure 9) and moisture content changes show up in the soil and rubble zones, where porosity is large. Changes in moisture content provide the basis for the ground penetrating radar difference tomograms, and simulated results are generally consistent with them, showing large increases in the soil, central fracture zone, and rubble zone (Peterson and Williams, 1999). Despite the strong signature of the column-bounding fractures in the liquid flow field, they do not show up as clearly as moisture content changes, due to their small porosity, thus making them difficult to image with geophysical methods such as ground penetrating radar. The gas flow field shows that most of the gas is purged from the subsurface during the initial stages of infiltration by lateral flow along high-permeability fractures and through the rubble zone. A few gas flow paths rise vertically within the infiltrating plume; these correspond to the gas bubbles observed in the pond during the infiltration test.

Figure 11 shows the simulated transient liquid saturation and capillary pressure response to ponding at selected locations in the model (identified in Figure 2). As in the pre-test simulations, there is a great variety in response, depending not only on the lithology at the monitoring location, but on the conditions along the entire pathway from the ground surface to the monitoring point. Similar behavior is observed in the field (Faybishenko et al., 1999).

The infiltration rate from the pond is shown in Figure 6. The overall decreasing trend is similar for the post-test calculation, the pre-test calculations, and the observed data. However, the post-test calculation levels off earlier than do the pre-test calculations, suggesting an earlier transition to gravity-driven flow. The shorter transient period may be the result of the non-uniform initial saturation distribution (Figure 8), which makes the medium seem less heterogeneous, as the segregation of liquid into rocks with strong capillary pressure tends to decrease the effective permeability of the materials with the highest intrinsic permeability and vice versa.

Although the ponded infiltration test lasted only two weeks, it is of interest to examine the long-term response to ponding, which is illustrated in Figures 12 and 13. Figure 12 shows the liquid saturation distribution and liquid flow field after one year of ponding, at which time the system is at steady-state. The lateral boundaries of the model, which are held at constant saturation, are not far enough away from the pond for the model to provide an accurate picture of the lateral extent of the infiltrated plume, but the wetting pattern beneath the pond may be reasonable. In contrast to the irregular saturation

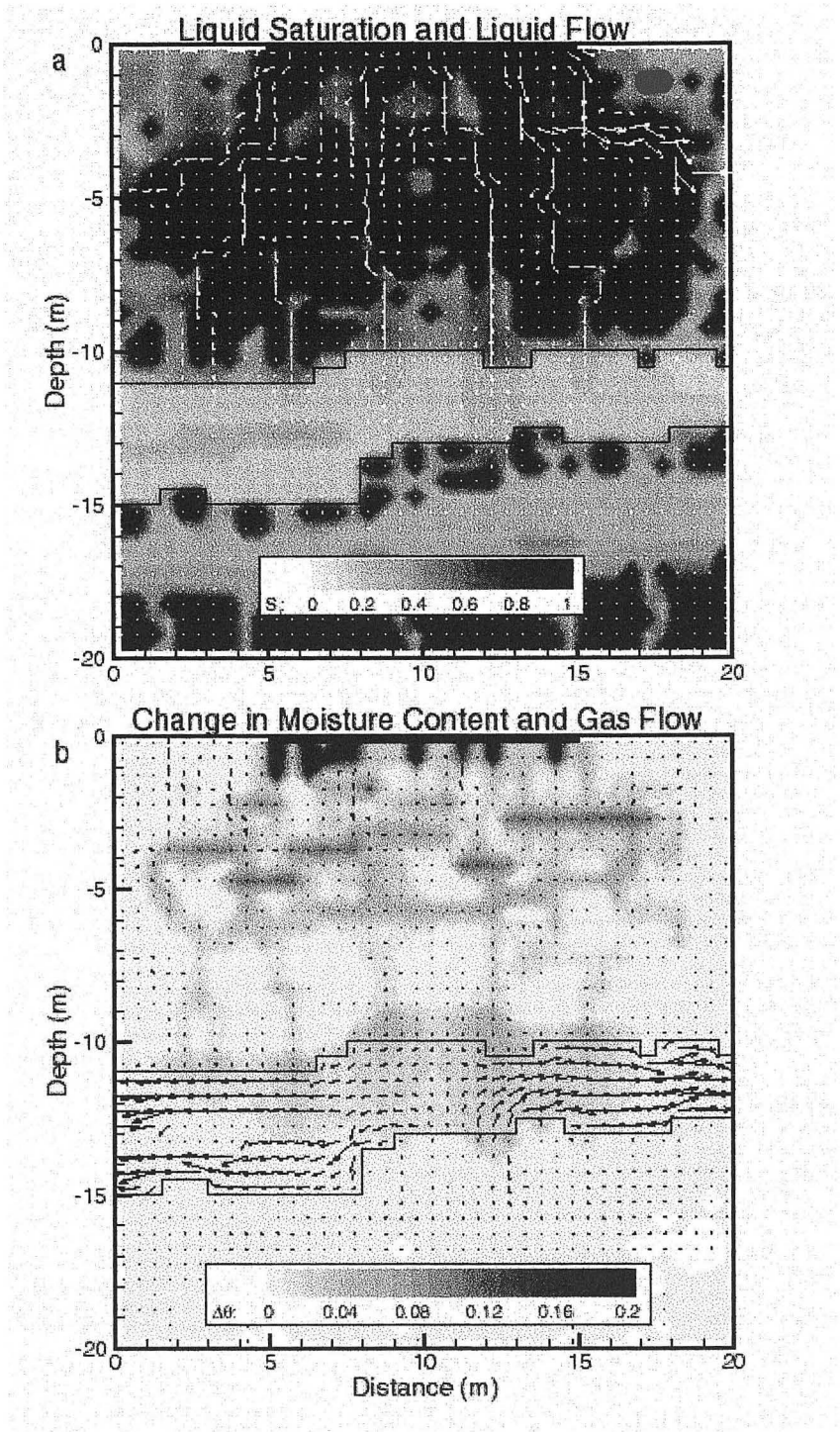

Figure 10. Simulated results after two weeks of ponded infiltration for the EOS3 post-test calculation: (**a**) liquid saturation and liquid flow field and (**b**) change in moisture content from the natural state (shown in Figure 8c) and gas flow field.

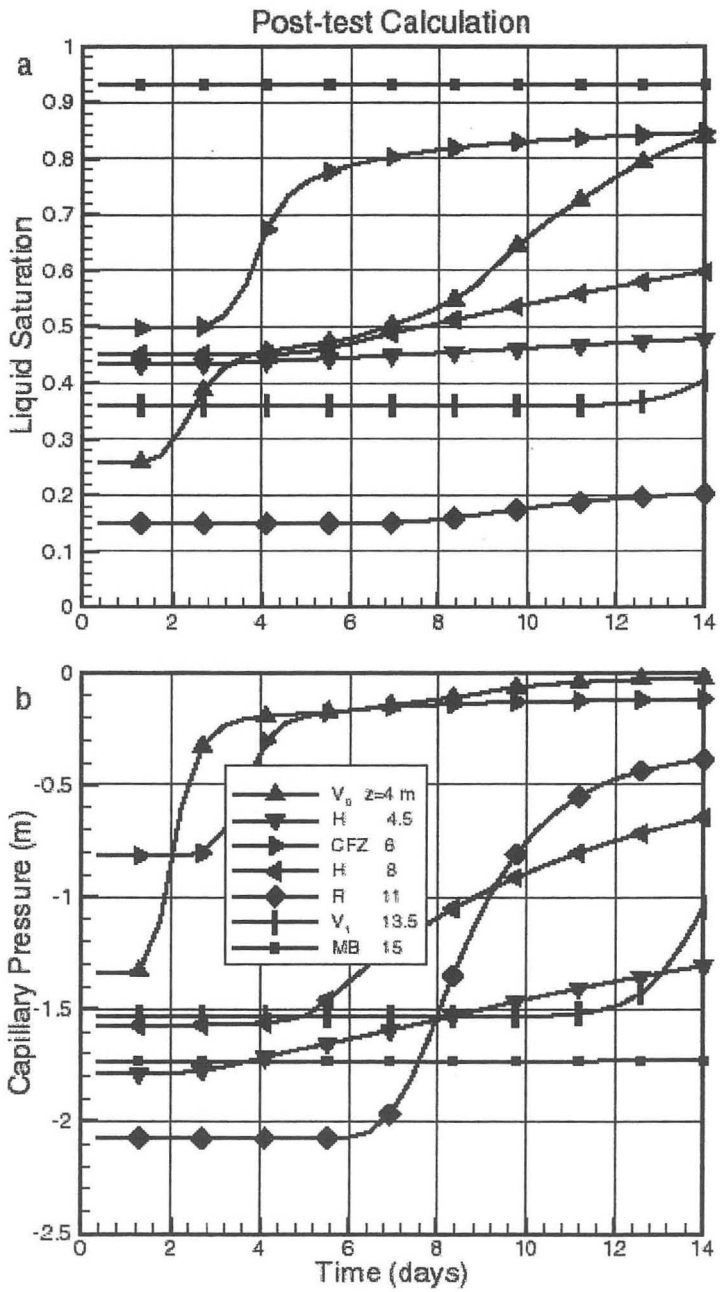

Figure 11. Simulated transient responses of (**a**) liquid saturation and (**b**) capillary pressure at selected locations (shown in Figure 2), for the EOS3 post-test calculation.

distribution after two weeks of ponding (Figure 10), the saturations in the highly fractured, upper 7 m of the model are now nearly uniformly high. The primary liquid flow paths remain largely the same, but slower flow from the primary vertical fractures to lower-permeability components of the system results in a more uniform saturation distribution.

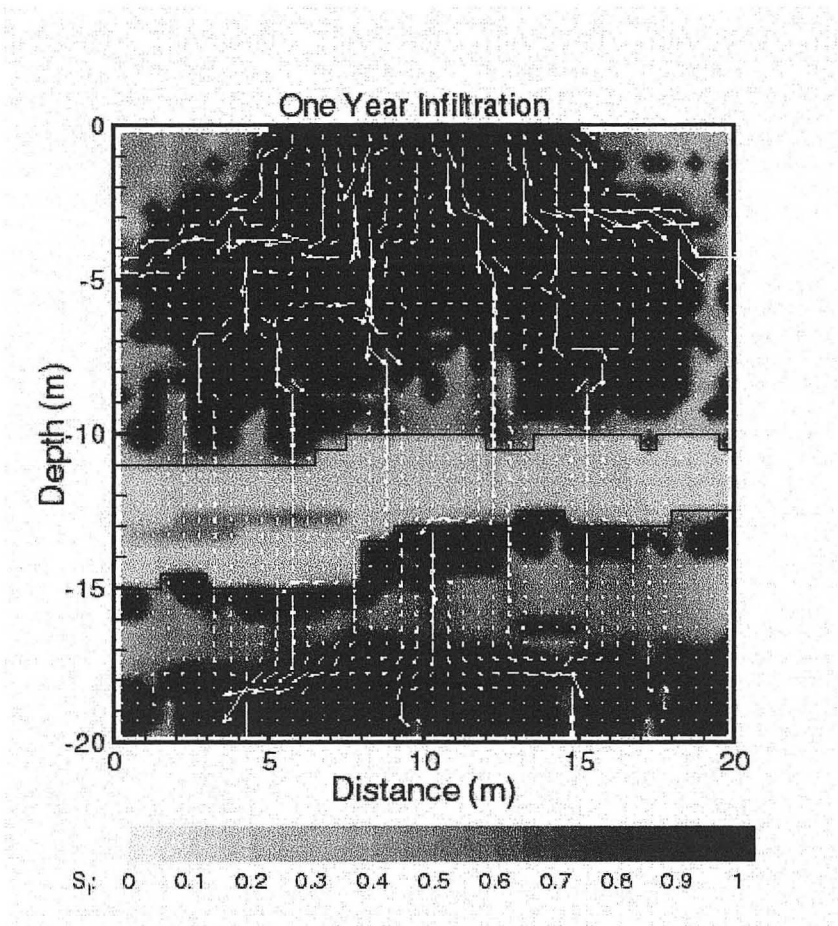

Figure 12. Simulated liquid saturation and liquid flow field after one year of ponded infiltration, for the EOS3 post-test calculation.

Figure 13 shows the infiltration rate from the pond as a function of time for the EOS3 calculation shown in Figure 12 and for an EOS9 calculation using the same model. As is also illustrated in Figure 6, the two cases show similar early-time behavior, with a decreasing infiltration rate, but the infiltration rate for the EOS3 case is smaller than that for the EOS9 case, due to entrapped air effects. For both cases, infiltration rate decreases until the infiltrating plume reaches the lower constant-pressure boundary of the model, at about one week. At this time, infiltration rate for the EOS9 case becomes constant and the system has essentially reached steady state. In contrast, at this same time the

infiltration rate for the EOS3 case begins to increase, due to the gradual removal of entrapped air, and does not reach a steady state until much later, almost one year. The flow out the lower boundary of the model, into the perched water body, is also shown in Figure 13. At steady state, the difference between infiltration rate from the pond and flow to the perched water body arises from lateral flow out of the model through the central fracture zone and the rubble zone.

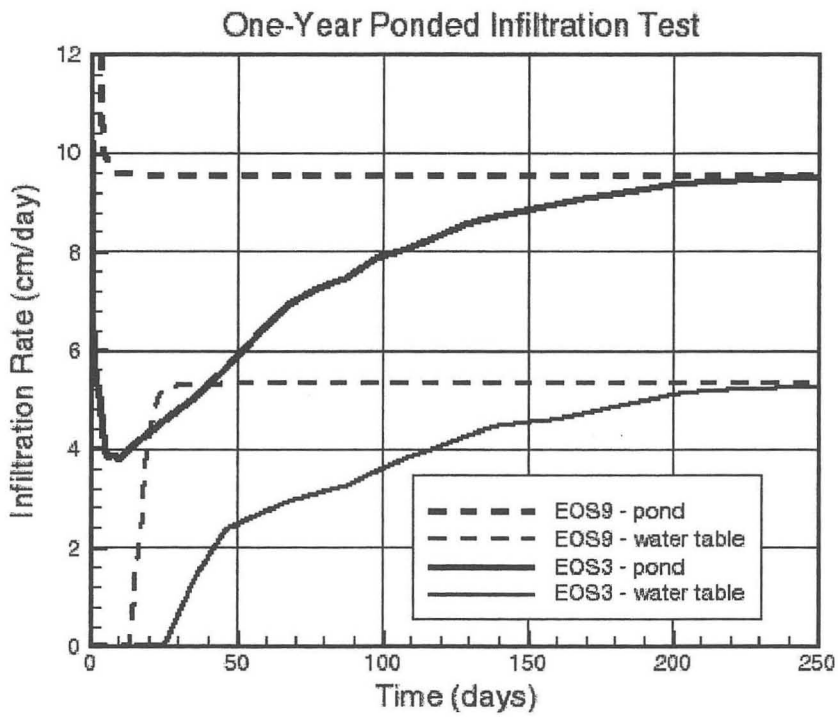

Fiigure 13. Simulated infiltration rate from the pond for one-year long ponded infiltration tests, for the EOS3 post-test calculation and for the same model using EOS9. Liquid flow rate out the lower boundary of the model, into an underlyingperched water body maintained at constant presuure, is also shown for each case.

The long-term behavior in the field may be rather different from that shown in Figure 13 if part of the infiltration rate decrease shown in Figure 6 arises from a decrease in permeability due to clogging of flow paths by fine particles that were mobilized during the test or by the growth of biofilms. Such a decrease in permeability, which is not included in the numerical model, would lessen or eliminate the late-time increase in infiltration rate shown in Figure 13.

Figure 14 shows the liquid saturation distribution and liquid flow field at a series of times during the drain-out period following a two-week ponded infiltration test. The drain-out proceeds irregularly, just as infiltration does, with the high-permeability pathways draining first. In contrast to the infiltration process, in which large changes in saturation occur at early times, drain-out appears to occur more gradually and is slower overall. This difference arises because of the different roles of large fractures, the fastest responding components of the system, during infiltration and drainage. During infiltration, the large fractures wet quickly and remain the dominant flow paths throughout infiltration. In contrast, during drain-out, these fractures drain quickly and thereafter do not control the drain-out process. The model predicts that the system will have returned to its undisturbed natural condition after about a year. However, field observations made just prior to the second ponded infiltration test (Faybishenko et al., 1999) suggest that even after one year, the site was still very wet. It is also noteworthy that while the pre-test and post-test simulations produce comparable predictions for the evolution of an infiltrating plume, they grossly differ in their predictions of drain-out, with pre-test simulations (not shown) predicting that it would take many years to return to undisturbed conditions. These findings suggest that drain-out may generally be more sensitive to initial and background conditions than infiltration is, and consequently more difficult to model.

4. Stochastic Representation of Subsurface Heterogeneity

The simplified deterministic approach for describing heterogeneity employed in this work requires more detailed geological information than is typically available, and is a very time-consuming procedure, making it an unusual technique for describing heterogeneous systems. A more widely used approach is to describe heterogeneity using geostatistics. In this section we compare results obtained with the deterministic model to those from a heterogeneous model created using traditional geostatistical techniques.

The first step in the geostatistical approach is to sample permeability values from the deterministic model as though they were field measurements, and use them to construct the probability density function (pdf) of the permeability distribution and directional variograms, which describe the correlation structure of the permeability distribution. We then use a correlated random field generator to create five permeability distributions that all have this same pdf and correlation structure. These permeability distributions are assigned to model grid blocks and used to simulate the infiltration test. The results of the five simulations are compared to each other and to the deterministic model.

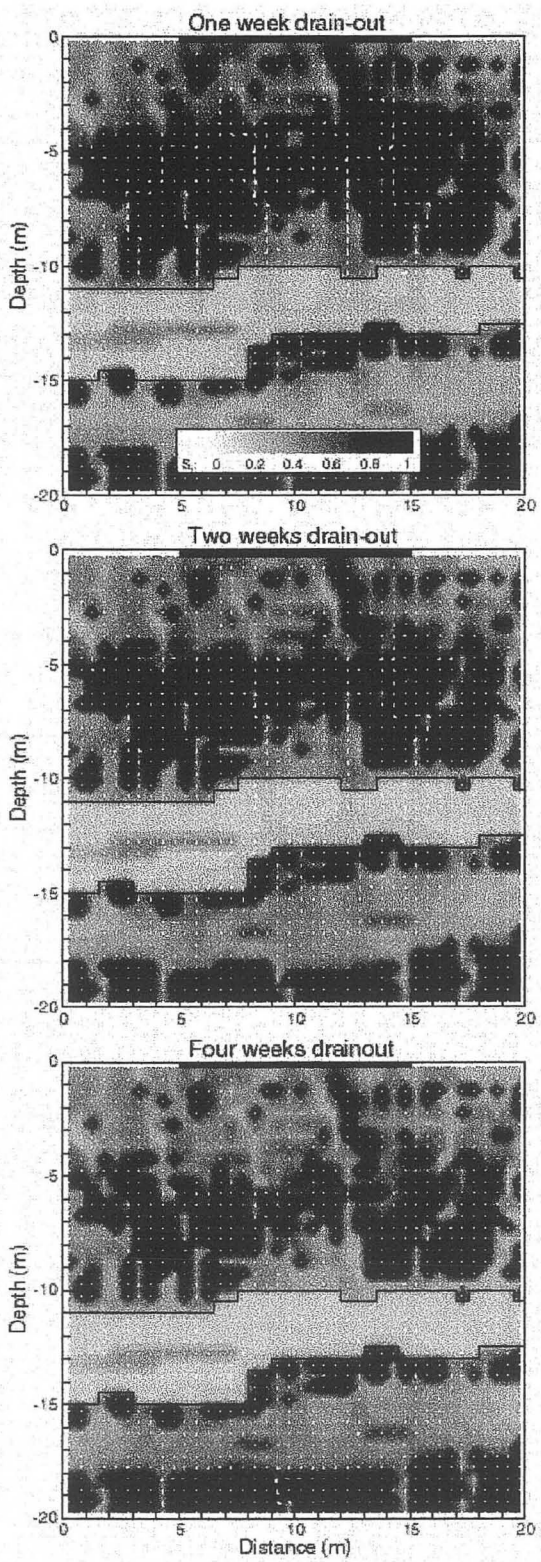

Figure 14. Simulated liquid saturation and liquid flow field at a series of times during the drain out period following a two-week infiltration test, for the EOS3 post-test calculation.

4.1 Construction of Stochastic Models

Figure 15 shows the permeability distribution for the deterministic model shown in Figure 2. The rubble zone permeability and geometry differ so greatly from the remainder of the medium that it is not included in the geostatistical analysis used to create the stochastic models but is represented deterministically, using the same properties and location as in the deterministic model. This approach is supported by the argument that even without the detailed geological information available at the Box Canyon site, rubble zones can be readily identified in well logs, making it unnecessary and in fact inappropriate to treat them stochastically at the present scale of investigation.

To determine the correlation structure, the portions of the permeability fields shown in Figure 15 above the rubble zone are sampled at two scales. At the 'grid scale' (0.5 m), the permeability value at every grid block in a 4 by 9 m region is used, to keep all small-scale variability possible. This procedure is repeated for four overlapping sub-regions of the model. A limitation on the number of data points the geostatistical analysis package can handle precludes analyzing all the permeability values from the entire model at once. At the 'well-field' scale, permeabilities measured at 2 m spacing in the horizontal direction and 0.5 m spacing in the vertical direction are used, to represent the kind of information typically available from a well field. Directional variograms are then constructed for the five data sets, using the public domain software Geostat Tool Box (Froidevaux, 1988). The two sampling strategies produce very similar variograms (shown below), which is encouraging.

The horizontal and vertical permeability distributions shown in Figure 15 are markedly different and in fact show rather different correlation structures (Figure 16), with the vertical permeability distribution showing a longer vertical correlation length and the horizontal permeability distribution showing a longer horizontal correlation length. The correlated random field generator employed, a modified version of CRFGEN (Datta-Gupta, personal communication, 1994), considers only a single value of permeability in each grid block, but allows different correlation structures in the vertical and horizontal direction. For the present problem, in which identifying preferential vertical flow is most important, we use the vertical permeability correlation structure shown in Figures 16c and 16d.

The pdf's for the horizontal and vertical permeability distributions above the rubble zone (Figure 17) are qualitatively similar, although the mean horizontal permeability is lower than the mean vertical permeability. As discussed above, we are most concerned with vertical flow, so we use the vertical permeability pdf from which to draw trial permeability values during construction of the correlated random field. Figure 17 shows that this pdf is far from log-normal, as is also evidenced by the color scheme of Figure 15. A log-normal pdf would produce a plot including equal numbers of pink and orange blocks as green and blue ones.

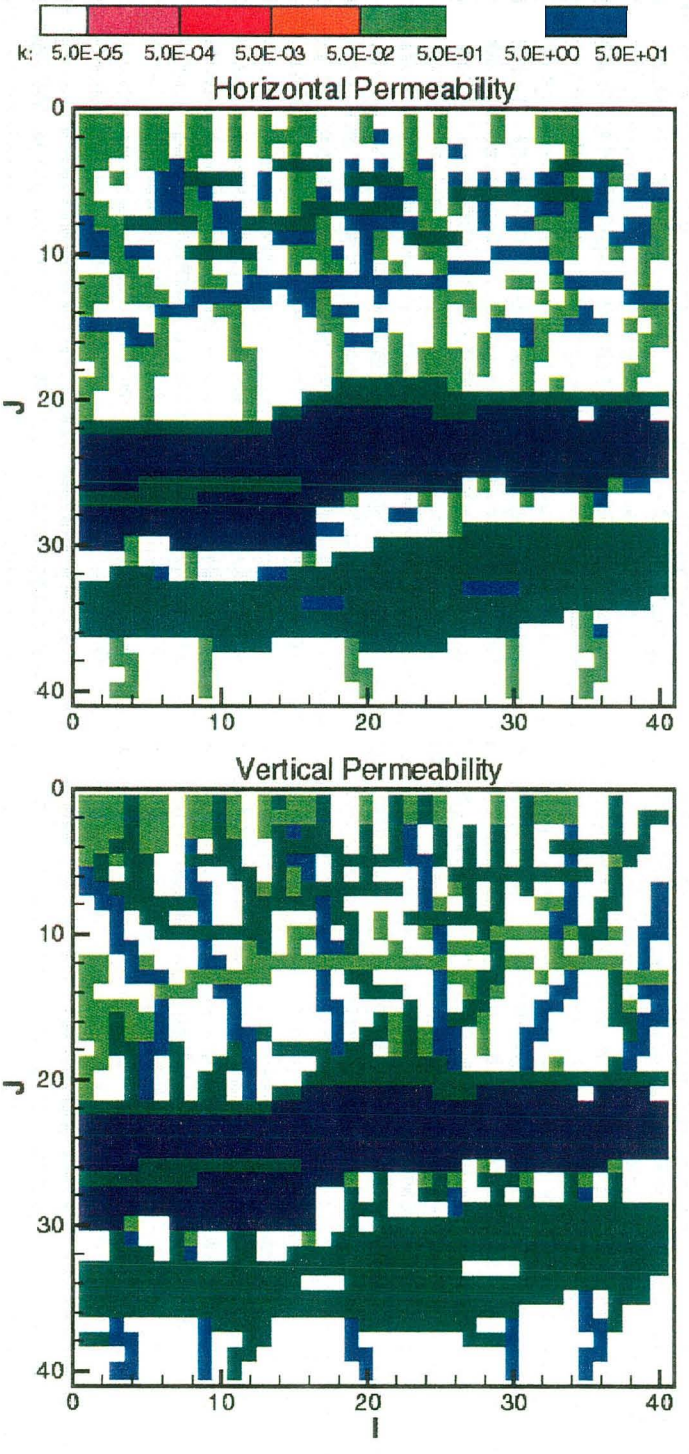

Figure 15. Permeability distributions for the deterministic model shown in Figure 2.

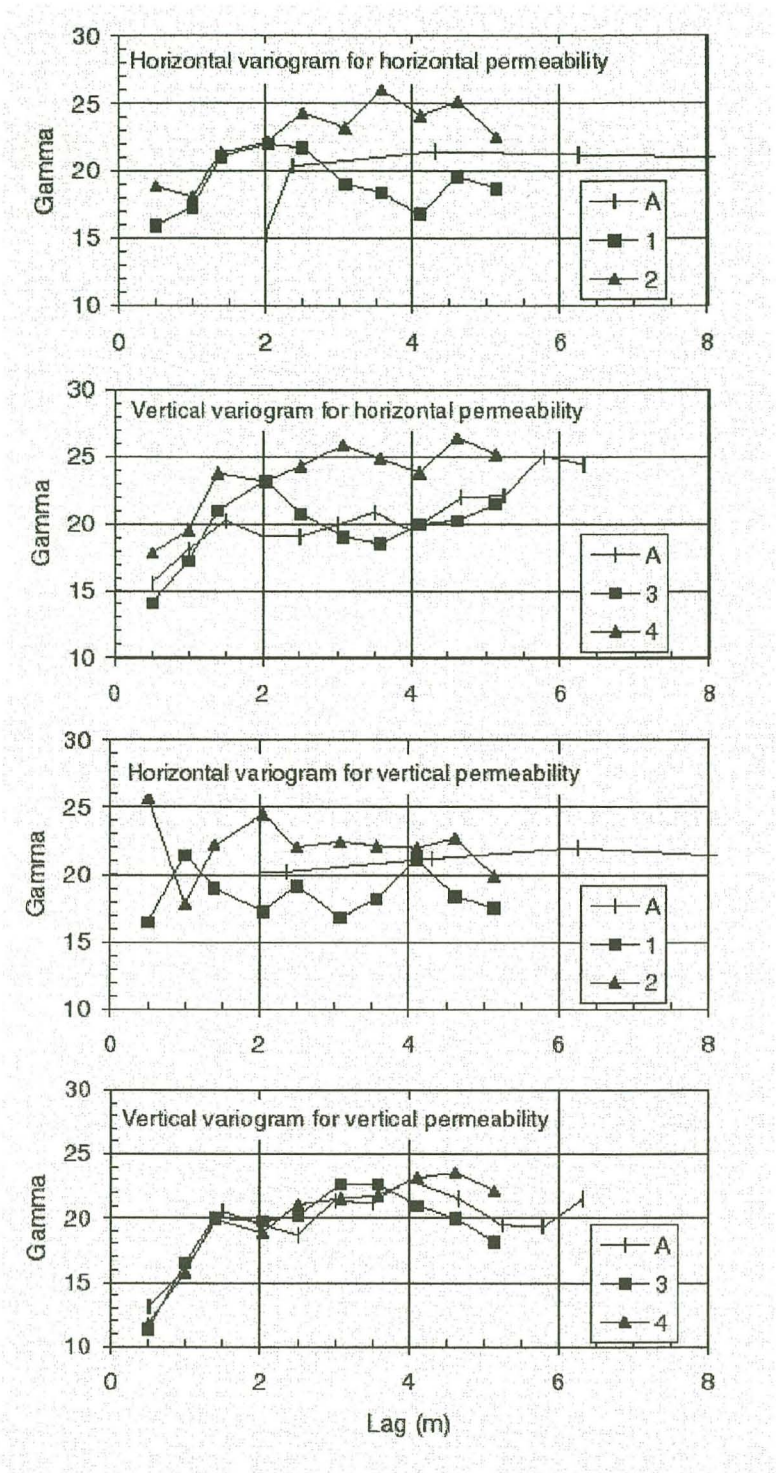

Figure 16. Directional variograms determined from the upper portions of the permeability fields shown in Figure 15. The curves labeled A use permeabilities sampled at 2-m horizontal intervals; the curves labeled 1-4 use different subsets of the permeability fields sampled at 0.5-m horizontal intervals. The vertical-permeability variograms labeled A are used in the random field generator.

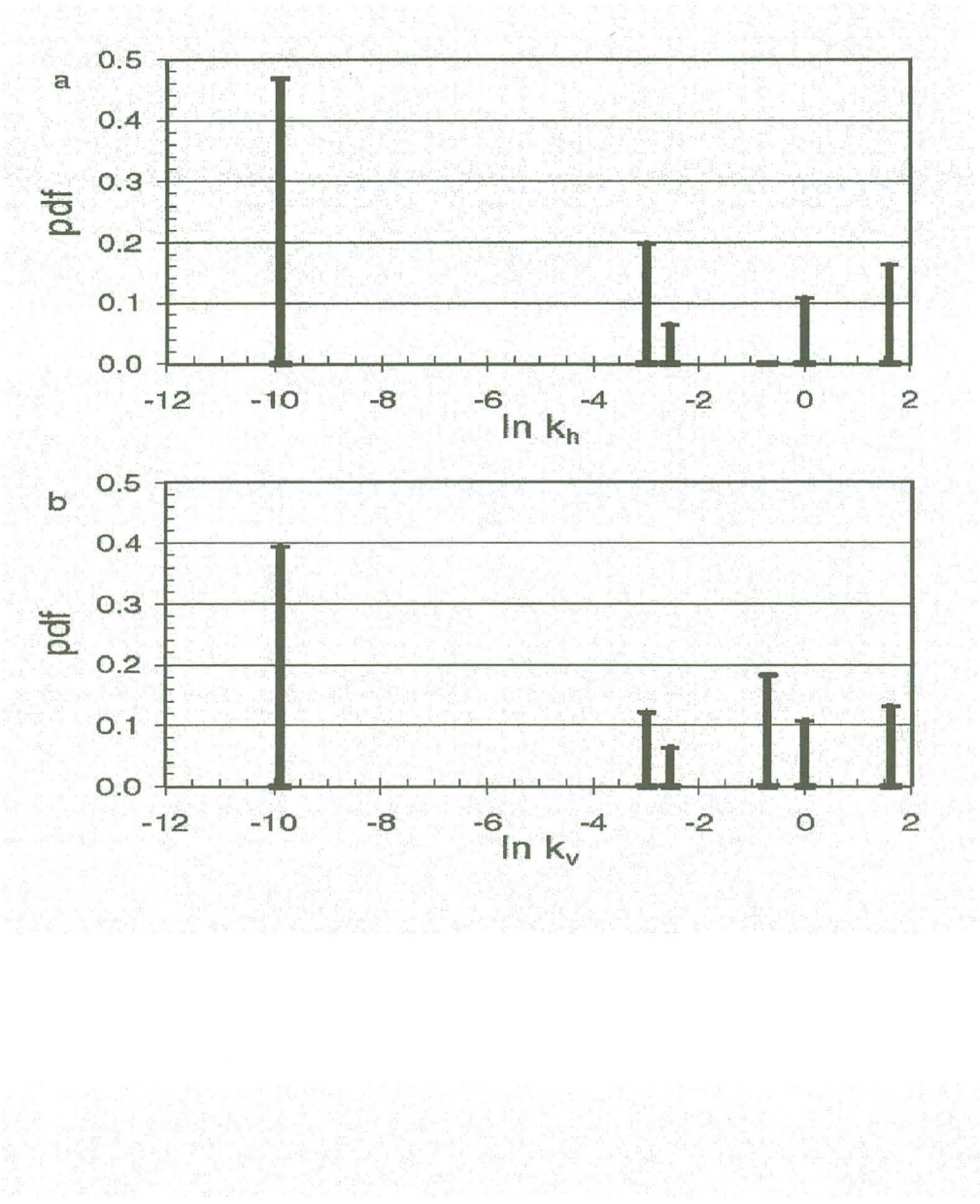

Figure 17. Probability density functions for the upper portions of the **(a)** horizontal and **(b)** vertical permeability distributions shown in Figure 15.

CRFGEN first creates a permeability distribution by drawing permeabilities at random from the specified pdf (Figure 17b). Using this permeability distribution, the directional variograms are determined and compared with the specified variograms (Figures 16c and 16d), and an objective function is constructed by summing the squared differences between the model and specified variograms. The optimization algorithm known as simulated annealing is used to minimize the objective function. At each iteration in the optimization, a trial permeability distribution is created by varying the permeability of a randomly chosen gridblock by drawing a new value from the specified pdf, new model variograms are determined, and the objective function is recomputed. The Metropolis algorithm (Metropolis et al., 1953) is used to determine whether or not the trial permeability distribution is accepted. The mean and standard deviation of the deterministic permeability distribution and the resulting stochastic distributions are shown in Table 3. There is some variability in the mean permeability of the stochastic models, but the standard deviations are all similar, the pdf's (not shown) all reproduce the general shape of the deterministic pdf, and the directional variograms all match those shown in Figures 16c and 16d within line thickness.

Visual inspection of the stochastically-generated permeability distributions (Figure 18) shows that they appear very different from the deterministic model, but generally similar to each other. The stochastic models do show the bimodal character of the deterministic model, in which there are high permeabilities (fractures, vesicular basalt) and low permeabilities (massive basalt), but nothing in between. This would not be possible if we had used a log-normal permeability distribution, a common assumption in geostatistics. Another important observation is that the stochastic models do not appear to capture the localized continuity of high-permeability features seen in the deterministic model, although they do honor the directional variogram data used to generate them.

4.2 Results of Ponded Infiltration Simulations

Figure 19 shows the liquid saturation distributions after two weeks of ponded infiltration for the five stochastic realizations and for a uniform permeability distribution. The EOS9 module of TOUGH2 is used for the stochastic-model simulations, making these results comparable to those shown in the second frame of Figure 4. Despite the qualitative similarity of the five stochastic permeability distributions, they produce a wide range of saturation distributions, making the predictive ability of the stochastic models quite small. Depending on the model used, one might predict that after two weeks, no water would have reached the rubble zone (Stoch 9) or that water would have reached the rubble zone, but largely beyond the footprint of the infiltration pond (Stoch 7 and Stoch 10). One could not say whether arrival at the rubble zone at a single point (Stoch 8 and Stoch 9) would be more likely than arrival over a broad area (Stoch 7 and Stoch 11). In contrast, the deterministic model predicts that after two weeks, water will have reached the rubble zone in a few discrete locations directly under the infiltration pond. Even with different locations for individual fractures, this general finding would remain true. Moreover, the pattern of flow in the deterministic model has a distinctly different character than in the stochastic models: it is roughly equally distributed among vertical column-bounding fractures, which are connected by horizontal features: vesicular lenses, fracture zones, and

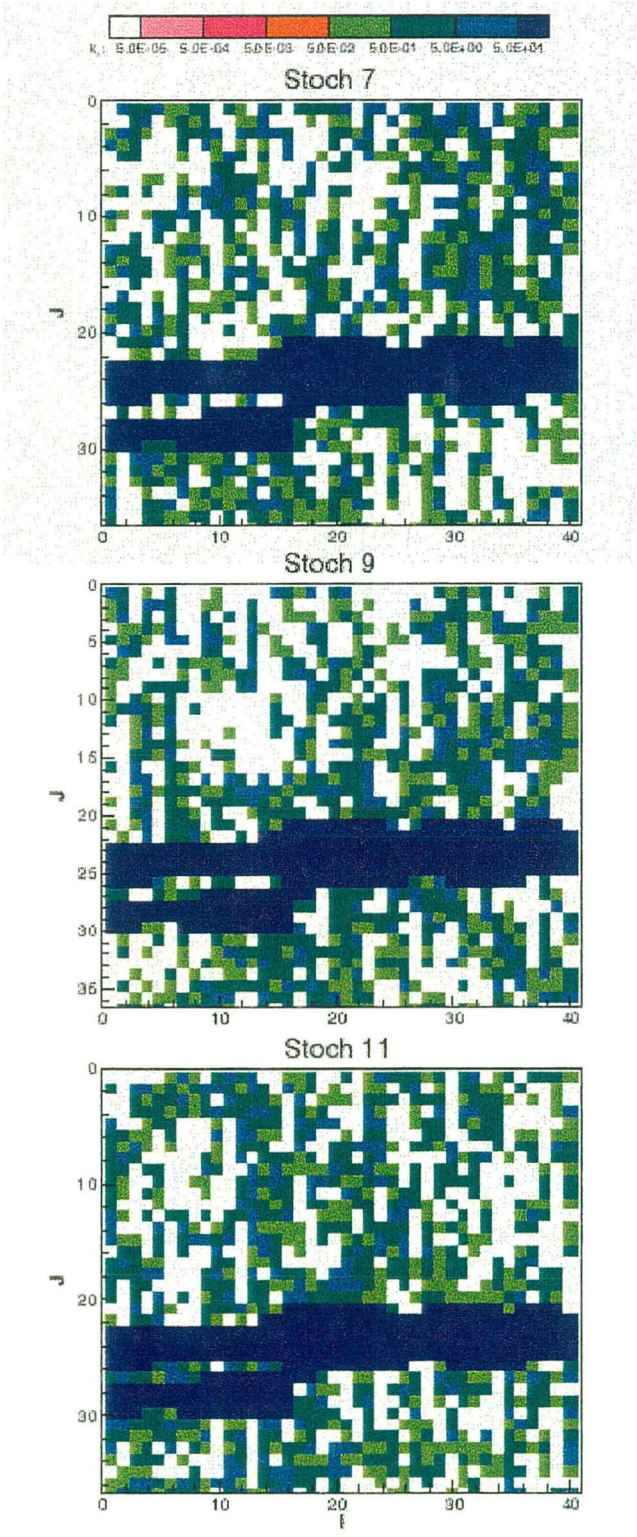

Figure 18. Vertical permeability distributions for three of the five realizations of the stochastic model. The other two realizations look similar.

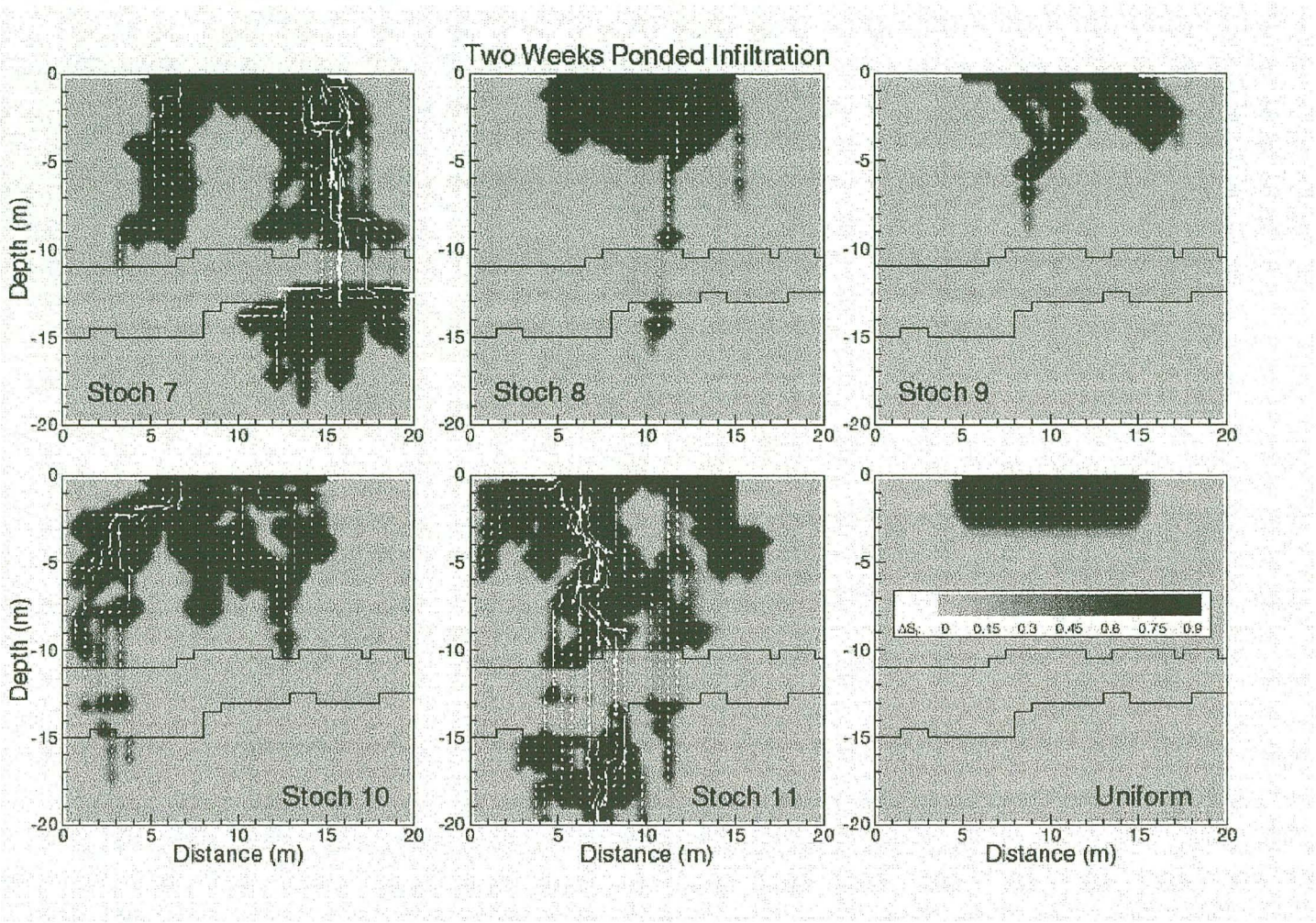

Figure 19. Simulated liquid saturation and liquid flow field after two weeks of ponded infiltration for the five stochastic models and the uniform model, using EOS9.

column-normal fractures. The characteristic spacing of these primary fracture flow paths gives the flow field an overall organized structure that is absent from the stochastic models. Despite matching the correlation structure of the permeability field, the stochastic models do not capture the geometric nature or the connectivity of the fracture pattern.

Given our usual lack of knowledge about the subsurface, the lack of predictability exhibited by the stochastic models is often appropriate. However, the goal of the present modeling exercise is to use all the available information to try to make good predictions rather than demonstrate that we cannot do so, and the deterministic model provides a preferred basis for this purpose. If it turns out that certain deterministic model predictions are wrong, we can vary parameters within the deterministic model while maintaining its geometric structure. For example, water actually arrives at the rubble zone sooner than two weeks after the start of ponding; this can be simulated by using a larger permeability or a smaller porosity for the primary vertical fractures. If we saw preferential flow paths with a spacing greater than the 5 m spacing of the primary vertical fractures (with present monitoring technology we cannot say whether this occurs or not), we could impose a variable permeability distribution within the primary vertical fractures, making some of them less permeable than others. In other words, we insist that the starting point for hydrogeological behavior is the fracture pattern observed in the field, but that other features, such as fracture infilling, aperture variation, etc. may also influence infiltration and may be incorporated within the model.

The infiltration rates for the stochastic models, the uniform model, and the deterministic model are shown in Figure 20. Again, variability among the stochastic models is quite large, consistent with the large range of sizes of infiltrated plumes shown in Figure 19. There is generally a correlation between infiltration rate and mean permeability (Table 3), with the notable exception of Stoch 8, which has the largest mean permeability and the smallest final infiltration rate. This point re-iterates the loss of information on flow-path connectivity that occurs in construction of a stochastic model from variograms, and the large role connectivity plays in controlling infiltration rate.A recurring theme of the field observations is that local lithology alone is not enough to redict what kind of response will be observed at a given point in the subsurface. Rather, local responses depend on the entire flow path from the surface (Faybishenko et al., 1999). This finding re-enforces the notion that fracture connectivity is of crucial importance in predicting the fate of contaminants migrating downward from the surface with infiltrating water, and consequently also re-enforces the notion that stochastic models constructed using variography are less likely to be successful in predicting observed behavior. Even with more sophisticated geostatistical analysis than used here, it remains a fact that much information about the connectivity of high-permeability flow paths is lost in the act of constructing variograms. Therefore, the information available to the resulting stochastic model is simply not sufficient to capture field behavior. Of course, there are other means of creating stochastic permeability distributions than through traditional variography.

One simple modification involves introducing the concept of a neighborhood into the simulated annealing algorithm used to generate the correlated random field, with acceptance rules that encourage connectivity implemented to augment the objective

function based on variograms (Liou et al., 1998). Based on the present study, methods that emphasize connectivity over correlation structure are expected to perform better.

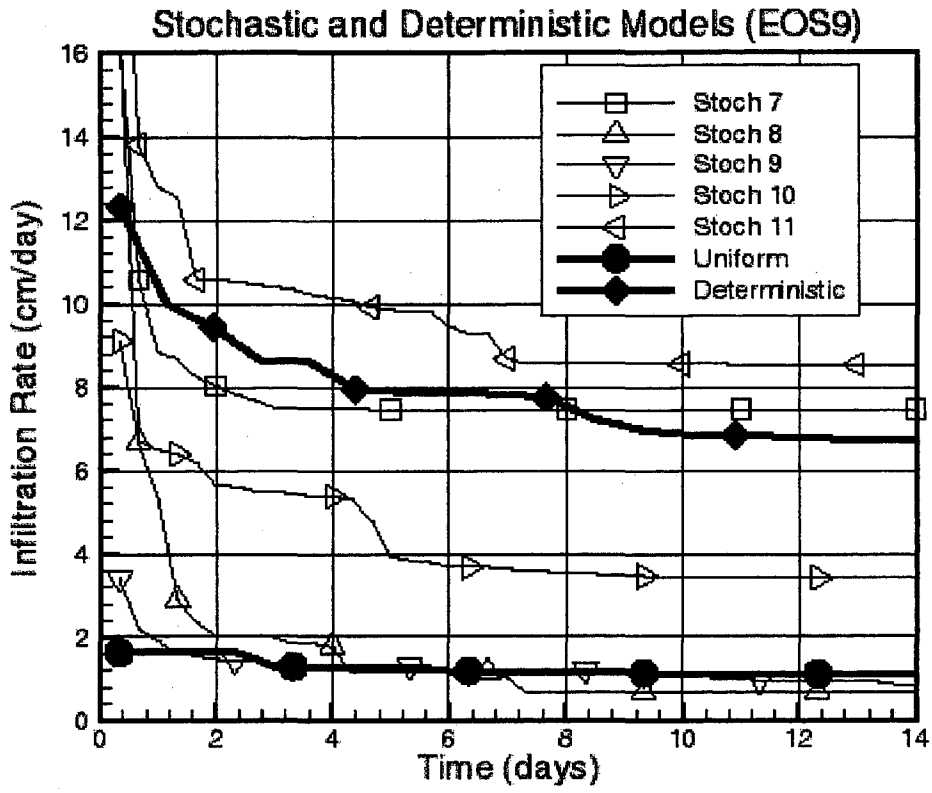

Fiigure 20. Simulated infiltration rate from the pond for the stochastic, uniform, and deterministic models, using EOS9.

5. Summary and Conclusions

Mathematical modeling of the ponded infiltration test conducted at Box Canyon has been done using the numerical simulator TOUGH2, which calculates fluid flow through geologic media. Simulations were conducted prior to the test to aid in experimental design, to study the importance of different factors affecting the test, and to predict the results of the test in order to assess our understanding of the salient features of infiltration through a fractured vadose zone. Simulations were conducted after the test to help explain the observed results, to assess the adequacy of the conceptual and numerical models, and to infer the importance of various physical processes and the values of material properties. The mathematical model uses an effective continuum approach, with half-meter resolution, enabling individual fractures to be resolved.

The pre-test simulations suggest that infiltration does not occur uniformly, but follows irregular flow paths through the highest-permeability features. Some lateral spreading occurs through vesicular zones and the central fracture zone, but flow through the rubble zone is nearly vertical. Entrapped air is shown to have a large effect, decreasing infiltration rate and creating a less uniform subsurface saturation distribution, whereas temperature effects are minimal. A sensitivity study suggests that capillary pressure changes the distribution of water in the subsurface, but it does not provide the primary control on infiltration rate from the pond.

The post-test simulation allows more realism to be included in the numerical model, by considering stable initial conditions in which gravity and capillary forces are balanced. The overall shape of the infiltrated plume is similar for both pre-test and post-test simulations, with the flow distribution controlled by the high-permeability features, suggesting that the greatly simplified pre-test simulations are useful for studying infiltration through the highly fractured Snake River Plain basalt. However, by incorporating capillarity the post-test simulation treats fracture/matrix interactions more accurately, and better illustrates how the system response occurs in the context of ambient conditions. This is important information to have when designing the monitoring component of a field test.

One of the key questions addressed by the modeling studies is how fracture-pattern characteristics and connectivity affect the pattern of water infiltration. We have found that strongly preferential gas-phase flow occurs through the sub-horizontal rubble zones that exist between basalt flows, because the permeability of these zones is several orders of magnitude higher than any other hydrological component at the site. In contrast, widespread lateral liquid flow through the rubble zone only occurs if there are no underlying vertical flow paths, because gravity plays such a dominant role in controlling liquid flow. For liquid infiltration from the ground surface, the highest permeability vertical flow paths are used. At the Box Canyon site, there are no vertical rubble zones near the ground surface, so the next most permeable flow paths, individual fractures and fracture zones, become the key hydrological component. Under background (low infiltration) conditions, the largest fractures are drained, leaving the highest effective permeability (intrinsic permeability times relative permeability) in the smaller fractures. Under ponded infiltration conditions, the largest fractures wet up and provide the primary vertical flow paths. The tributary structure of the fractures, shown in Figure 3 and described in more detail in Faybishenko et al. (1999), causes the liquid flow to undergo a funneling process with depth, which has been indirectly observed in the field (Faybishenko et al., 1999).

A comparison of the deterministic modeling approach with a more traditional stochastic approach for representing subsurface heterogeneity suggests that the stochastic approach is less successful in predicting field behavior because too much information about fracture connectivity is lost in the geostatistical analysis. Overall, the deterministic model results have been consistent with field observations, and modeling has been an effective tool to assess our understanding and aid in experimental design.

Appendix: Governing Equations for Flow and Transport

The governing equations for fluid and heat flow for a multi-component system consist of a mass balance for each component m (w for water, t for tracer, a for air) and an energy balance (m = e):

$$\frac{\partial M_m}{\partial t} + \nabla \cdot Q_m = 0, \tag{A.1}$$

where the mass accumulation terms (M_m with m = w, t, a) are given by

$$M_m = \phi(S_l \rho_l X_l^m + S_g \rho_g X_g^m) \tag{A.2}$$

and the energy accumulation term (M_e) is given by

$$M_e = (1-\phi)C_r T + \phi(S_l \rho_l u_l + S_g \rho_g u_g). \tag{A.3}$$

The mass flux terms (Q_m with m = w, t, a) are given by the sum of the mass flux in each phase β (l for liquid and g for gas):

$$\begin{aligned} Q_m &= Q_l^m + Q_g^m \\ &= -\frac{k k_{rl} \rho_l X_l^m}{\mu_l}(\nabla P_l - \rho_l g) - \frac{k k_{rg} \rho_g X_g^m}{\mu_g}(\nabla P_g - \rho_g g) + D_{va} \rho_g \nabla X_g^m, \end{aligned} \tag{A.4}$$

and the energy flux term (Q_e) is given by

$$Q_e = -\lambda \nabla T + \sum_{\substack{\beta=l,g \\ m=w,t,a}} h_\beta^m Q_\beta^m. \tag{A.5}$$

In the above equations, ϕ is porosity, S is saturation, ρ is density, X_β^m is the mass fraction of component m in phase β, C_r is rock volumetric heat capacity, T is temperature, u_β is the internal energy of the phase β, k is intrinsic permeability (in general a tensor), $k_{r\beta}$ is the relative permeability of phase β, μ is viscosity, P is pressure, g is gravitational acceleration, D_{va} is the binary diffusion coefficient for water vapor and air, λ is thermal conductivity, and h_β^m is the enthalpy of component m in phase β. These equations are augmented by the closure conditions $S_l + S_g = 1$, $X_\beta^w + X_\beta^t + X_\beta^a = 1$ for each phase β, $P_g = P_v + P_a$, and $P_c = P_l - P_g$, where P_v and P_a are the partial pressures of water vapor and air, respectively, in the gas phase, and P_c is capillary pressure.

Relative permeabilities and capillary pressure are specified as functions of liquid saturation. The following functional forms are used in the present work (slightly more general versions may be found in the TOUGH user's guide (Pruess, 1987)). In the following expressions, the saturation S^* is defined as $S^* = (S_l - S_{lr})/(1 - S_{lr})$, where, S_{lr} is the residual liquid saturation, defined as the saturation below which liquid is immobile.

Corey (1954) $\quad k_{rl} = S^{*4}$ for $S^*>0$, 0 otherwise (A.6)

$k_{rg} = (1 - S^*)^2(1 - S^{*2})$ for $S^*>0$, 1 otherwise

Power-law $k_{rl} = S^{*n}$ with $n = 5$ for $S^*>0$, 0 otherwise (A.7)

$k_{rg} = (1-S^*)^n$ with $n = 5$ for $(1-S^*)<1$, 1 otherwise.

van Genuchten (1980) $k_{rl} = S^{*1/2}[1 - (1 - S^{*1/m})^m]^2$ for $S^*>0$, 0 otherwise (A.8)

$k_{rg} = 1 - k_{rl}$

$P_c = -P_{c0}[S^{*-1/m} - 1]^{1-m}$ for $S^*>0$ and $P_c<P_{cmax}$, P_{cmax} otherwise

Acknowledgments

The careful review of this work by B. Faybishenko, S. Finsterle, K. Pruess, and A. Simmons is greatly appreciated. I have benefited from fruitful discussions throughout the course of these studies with Boris Faybishenko, Jane Long, and John Peterson. It has been a pleasure to use the elegant computer programs written by Karsten Pruess and Stefan Finsterle. This work was supported by the Assistant Secretary for Environmental Restoration and Waste Management, EM-50, Office of Technology Development, Characterization, Monitoring and Sensor Technology Program, of the U.S. Department of Energy under Contract No. DE-AC03-76SF00098.

References

Aydin, A. and J. Lore, Characterization of the fracture patterns in basalt flows at Box Canyon, Idaho, internal report, Lawrence Berkeley National Laboratory, Berkeley, CA, 1997.

Baca, R.G., S.O. Magnuson, H.D. Nguyen, and P. Martian, A modeling study of water flow in the vadose zone beneath the Radioactive Waste Management Complex, Rep. EGG-GEO-10068, Idaho National Engineering Laboratory, Idaho Falls, Idaho, 1992

Barenblatt, G.E., I.P. Zheltov, and I.N. Kochina, Basic concepts in the theory of homogeneous liquids in fissured rocks, J. of Applied Mathematics (USSR), 24, 5, 1286-1303, 1960.

Benito, P.H., P. Cook, B. Faybishenko, B. Freifeld, and C. Doughty, Analog site for fractured rock characterization: Box Canyon pneumatic connectivity study, preliminary data analysis, Rep. LBNL-42359, Lawrence Berkeley National Laboratory, Berkeley, CA, 1998.

Bishop, C.W., Hydraulic properties of vesicular basalt, M.Sc. Thesis, Dept. of Hydrology and Water Resources, University of Arizona, Tucson, AZ, 117 pp., 1991.

Corey, A.T., The interrelation between gas and oil relative permeabilities, Producers Monthly, 19, 38-41, 1954.

Doughty, C. Investigation of conceptual and numerical approaches for evaluating gas, moisture, heat, and chemical transport in fractured unsaturated rock, in press, J. Cont. Hydrology, 1998.

Edwards, A.L., TRUMP: A computer program for transient and steady state temperature distributions in multidimensional systems, National Technical Information Service, National Bureau of Standards, Springfield, VA, 1972.

Faybishenko, B., Two field experiments for ponded infiltration in foundation pits, presented at AGU 13th Annual Hydrology Days, Colorado State University, Fort Collins, Colorado, March 30-April 2, 1993.

Faybishenko, B.A., Hydraulic behavior of quasi-saturated soils in the presence of entrapped air: laboratory experiments, Water Resources Res., 31(10), 2421-2435, 1995.

Faybishenko, B., C. Doughty, M. Steiger, J.C.S. Long, T.R. Wood, J.S. Jacobsen, J. Lore, and P.T. Zawislanski, Conceptual model of the geometry and physics of fluid flow and chemical transport in unsaturated fractured basalt: Box Canyon Site, Idaho, Rep. LBNL-40629, Lawrence Berkeley Laboratory, Berkeley, CA, 1999.

Faybishenko, B., P. Jordan, M. Mesa, D. Burgess, C. Knutson and B. Sisson, Lithological conditions at the Box Canyon site: results of drilling, coring, and open borehole measurements - 1995 - 1997 data report, Rep. LBNL-40182, Lawrence Berkeley National Laboratory, Berkeley CA, 1998.

Faybishenko, B., R. Salve, P. Zawislanski, C. Doughty, K.H. Lee, P. Cook, B. Freifeld, J. Jacobsen, J.B. Sisson, J. Hubbell, and K. Dooley, Ponded infiltration test at the Box Canyon site: Data report and preliminary analysis, Rep. LBNL-40183, Lawrence Berkeley National Laboratory, Berkeley, CA, 1998b.

Froidevaux, R., Geostat tool box primer, Version 1.00, developed in collaboration with A.G. Journel, Stanford University, 1988.

Grossenbacher, K.A. and B. Faybishenko, Thermal effects in spacing of columnar joints in basalt: variations with depth, Rep. LBL-38060, Lawrence Berkeley National Laboratory, Berkeley, CA, 1995.

Knutson, C.F., K.A. McCormick, J.C. Crocker, M.A. Glenn, and M.L. Fishel, 3D RWMC vadose zone modeling, Rep. EGG-RD-10246, Idaho National Engineering Laboratory, Idaho Falls, Idaho, 1992.

Liou, T.-S., K. Pruess, and Y. Rubin, Numerical simulation of experiments on water seepage in unsaturated, heterogeneous fractures, in Proceedings of the TOUGH Workshop '98, Rep. LBL-41995, Lawrence Berkeley National Laboratory, Berkeley, CA, 1998.

Long, J.C.S., C. Doughty, B. Faybishenko, A. Aydin, B. Freifeld, K.A. Grossenbacher, P. Holland, J. Horsman, J.S. Jacobsen, T.M. Johnson, K.-H. Lee, J. Lore, K. Nihei, J.E. Peterson, Jr., R. Salve, J.B. Sisson, B. Thapa, D. Vasco, K.H. Williams, T.R. Wood, and P. Zawislanski, Analog Site for Fractured Rock Characterization, Annual Report FY 1995, Rep. LBL-38095, Lawrence Berkeley National Laboratory, Berkeley, CA, 1995.

Metropolis, N., A. Rosenbluth, M. Rosenbluth, A. Teller, and E. Teller, Equations of state calculations by fast computing machines, Journal of Chemical Physics, 21, 1087-1092, 1953.

Narasimhan, T.N. and P.A. Witherspoon, An integrated finite difference method for analyzing fluid flow in porous media, Water Resources Res., 12(1), 57-64, 1976.

Peterson, J.E., Jr. and K.H. Williams, Ponded infiltration test in fractured basalt at the Box Canyon site: ground penetrating radar imaging of moisture content, Rep. LBNL-40631, Lawrence Berkeley Laboratory, Berkeley, CA, 1999.

Peterson, J.E., Jr. and K.H. Williams, Ground penetrating radar results at the Box Canyon site: 1996 survey as part of infiltration test, Rep. LBL-40915, Lawrence Berkeley National Laboratory, Berkeley, CA, 1997.

Pruess, K., TOUGH user's guide, Rep. LBL-20700, Lawrence Berkeley Laboratory, Berkeley, CA, 1987.

Pruess, K., TOUGH2 - A general-purpose numerical simulator for multiphase fluid and heat flow, Rep. LBL-29400, Lawrence Berkeley Laboratory, Berkeley, CA, 1991.

Pruess, K., Ed., Proceedings of the TOUGH Workshop '95, Rep. LBL-37200, Lawrence Berkeley Laboratory, Berkeley, CA, 1995.

Pruess, K., Ed., Proceedings of the TOUGH Workshop '98, Rep. LBL-41995, Lawrence Berkeley National Laboratory, Berkeley, CA, 1998.

van Genuchten, M.Th., A closed-form equation for predicting the hydraulic conductivity of unsaturated soils, Soil Sci. Soc. Amer. J.,44, 892-898, 1980.

Warren, J.E. and P.J. Root, The behavior of naturally fractured reservoirs, Soc. Pet. Eng. J., 228, 245-255, 1963.

Wood, T.R. and G.T. Norrell, Integrated large-scale aquifer pumping and infiltration tests, Rep. INEL-96/0256, Idaho National Engineering Laboratory, Idaho Falls, Idaho, 1996.

Wu, Y.S., C.F. Ahlers, P. Fraser, A. Simmons and K. Pruess, Software qualification of selected TOUGH2 modules, Rep. LBNL-39490, Lawrence Berkeley National Laboratory, Berkeley, CA, 1996.

Table 1. Material properties used for the numerical simulations of the 1996 ponded infiltration test.

Material name	Porosity	Horizontal permeability (10^{-15} m^2)	Vertical permeability (10^{-15} m^2)	Capillary pressure strength (Pa) for post-test calculations
Rubble zone (R)	0.50	10^6	10^6	24
Primary vertical fracture (V_0)	0.08	50	5000	230
Central fracture zone - vesicular (CFZ)	0.15	5000	50	1270
Central fracture zone - non-vesicular (CFZ_{nv})	0.10	5000	50	1270
Secondary vertical fracture (V_1)	0.07	0.05	500[a]	850
Horizontal fracture (H)	0.05	5000	0.05	1800
Other fracture (O)	0.05	50	50	1800
Vesicular basalt (VB)	0.20[b]	1000[b]	1000[b]	610
Soil (S)	0.50[c]	78[c]	78[c]	2,040
Massive basalt (MB)	0.05	0.05	0.05	39,500

[a]Knutson et al. (1992)
[b]Bishop (1991)
[c]Baca et al. (1992)

Permeability and porosity values for the different materials estimated based on a hierarchical fracture structure (B. Faybishenko, personal communication, 1996), unless otherwise noted.

Pre-test: Corey (1954) relative permeability functions with S_{lr} = 0.12 and zero capillary pressure, unless otherwise noted in Table 2.

Post-test: Power-law relative permeability functions with an exponent of n = 5 and S_{lr} = 0.1; van Genuchten (1980) capillary pressure with m = 0.3 and capillary pressure strength ($1/\alpha$) inferred by calibration to natural-state data assuming a background infiltration rate of 10 cm/yr.

Table 2. Sensitivity studies conducted prior to the 1996 ponded infiltration test.

Case	EOS	Features	Infiltration rate* (cm/day)
13	9	Base case with no entrapped air	6.6
16	3	Base case with entrapped air	4.9
17	3	Air more mobile (van Genuchten (1980) relative permeabilities with $k_{rg}=1-k_{rl}$)	5.8
26	3	Air and water more mobile (linear relative permeabilities)	5.8
19	9	Fracture porosities decreased by about a factor of 10	6.5
20	9	Fracture permeabilities increased by a factor of 10	30.5
18	9	Fractures don't go to ground surface	4.3
24	3	Fractures are soil-filled below rubble zone	4.9
25	3	Fractures replaced by massive basalt below rubble zone	4.9
22	3	Non-isothermal case: pond water is 20°C, initial subsurface temperature is 10°C	6.4
28	9	van Genuchten (1980) relative permeability and capillary pressure with $S_{lr} = 0.1$, $m = 0.3$ and $P_{c0} \sim k^{-1/2}$	6.6

*after 21 days of ponded infiltration; infiltration rate is approximately steady

Table 3. Parameters of deterministic and stochastic models, and resulting infiltration rates. These models all use EOS9.

Model	Mean log permeability (10^{-12} m^2)	Standard deviation of log permeability (10^{-12} m^2)	Infiltration rate* (cm/day)
Deterministic	-4.34	4.66	6.6
Stoch 7	-4.02	4.62	7.4
Stoch 8	-3.89	4.56	0.7
Stoch 9	-4.36	4.59	0.9
Stoch 10	-4.08	4.56	3.4
Stoch 11	-4.06	4.60	8.5
Uniform	-4.34	0	1.1

*after 14 days of ponded infiltration; infiltration rate is approximately steady

Ernest Orlando Lawrence Berkeley National Laboratory
One Cyclotron Road | Berkeley, California 94720

Prepared for the U.S. Department of Energy under Contract No. DE-AC03-76SF00098